On Microstructural Analysis of Porous Media Existing in Fuel Cells Using the Lattice Boltzmann Method

Espinoza Andaluz, Mayken

2015

LUNDS UNIVERSITET
Lunds Tekniska Högskola

On Microstructural Analysis of Porous Media Existing in Fuel Cells Using the Lattice Boltzmann Method

Mayken Stalin Espinoza Andaluz

Thesis for the degree of Licentiate of Philosophy, 2015

Division of Heat Transfer
Department of Energy Sciences
Faculty of Engineering (LTH)
Lund University

www.energy.lth.se

Division of Heat Transfer
Department of Energy Sciences
Faculty of Engineering (LTH)
Lund University
Box 118, SE-221 00, Lund, Sweden

ISRN LUTMDN/TMHP-15/7093-SE
ISSN 0282-1990
ISBN 978-91-7623-593-5

Abstract

This Licentiate thesis aims to gain understanding related to the fluid behavior in porous media existing in fuel cells (FCs) at microscale. In order to achieve this; the widely used methodology for solving transport problems in porous media has been applied, i.e., the lattice Boltzmann method (LBM). LBM presents several advantages to solve transport problems where the microstructural architecture is complex.

The introductory part presents the scope of the thesis and the different parts included in the document. Different characteristics of the FCs are given, as well as the parts where the porous media are found within the FCs. The mechanism of energy conversion for two selected kinds of FCs is explained, and the simplified electrochemical reactions involved in such conversion are presented.

The second part of the thesis corresponds to the LBM explanation and the solution of several physical problems. The simulations are carried out at different Reynolds numbers in order to prove the ability of LBM for solving transport problems at different regimes, and to get knowledge about the effects of the boundary conditions implemented. The simulation results performed in this part are corresponding to macroscale. The momentum and energy equations form the base for the results obtained using the LBM. All simulations are validated with corresponding previous studies, which show a relatively high accuracy of the method.

Finally, simulation results of the fluid behavior in porous media are presented. Both, randomly generated and a reconstructed porous domain from a real image are analyzed. Microstructure parameters such as porosity, gas-phase tortuosity and permeability are obtained after using the LBM. The results obtained are compared with previous studies, and the opportunity for future work is detailed in the last chapter.

Keywords: Porous media, Lattice Boltzmann method, Microscale, Fuel cell, Porosity, Gas-phase tortuosity

Sammanfattning

Denna licentiatavhandling syftar till en ökad förståelse för vätskebeteende i de porösa material som finns i bränsleceller (BCer) i en mikroskala. För att uppnå detta; har lattice Boltzmann metoden (LBM), används för att beräkna transportproblem i porösa medier. LBM presenterar flera fördelar med att lösa transportproblem där mikroarkitekturen är komplex.

Inledningen presenterar omfattningen av avhandlingen och de olika delarna som ingår. Olika egenskaper hos BCer en ges, samt mer specifikt för de delar där de porösa medierna återfinns inom BCerna. Mekanismen för energiomvandling för två utvalda typer av BCer förklaras, och de förenklade elektrokemiska reaktioner som är inblandade i sådan omvandling presenteras.

Den andra delen av avhandlingen förklarar LBM och lösningen av flera fysiska transportproblem. Simuleringarna genomförs för olika Reynolds nummer för att bevisa förmågan hos LBM att lösa transportproblem med olika egenskaper, och för att få kunskap om de randvillkoren. Simuleringsresultaten som presenteras i denna del motsvarar makroskala. Flödes och energiekvationerna utgör basen för de resultat som uppnåtts med hjälp av LBM. Alla simuleringar valideras med motsvarande tidigare studier, som visar en relativt hög noggrannhet av metoden.

Slutligen presenteras simuleringsresultat hos vätskebeteende i porösa medier. Både en slumpmässig och en rekonstruerad porös domän från en verklig bild analyseras. Mikroparametrar såsom porositet, gasfastortositet och permeabilitet erhålls med LBM. De erhållna resultaten jämförs med tidigare studier, och möjligheter för det fortsatta arbetet ges i det sista kapitlet.

Nyckelord: Porösa medier, Lattice Boltzmann metoden, Mikroskala, Bränslecell, Porositet, Gasfastortositet

Acknowledgements

This work has been carried out at the Division of Heat Transfer, Faculty of Engineering (LTH), Department of Energy Sciences, Lund University, Lund, Sweden.

I would like to express my gratitude to my supervisors Docent Martin Andersson and Professor Bengt Sundén for giving me the opportunity of doing my PhD studies in the Department of Energy Sciences at Lund University. Their guidance, academic confidence and all the support that I have received from them have been crucial during my study period in Sweden. I am also grateful to Professor Jinliang Yuan for his help and good discussions during my studies.

In addition, I would like to express my deep appreciation to all my fellow PhD students and administrators at the Department of Energy Sciences for good working environment and cooperation during this time.

Finally, a special thanks to my family. Words cannot express how grateful I am to my parents for all of the sacrifices that you have made on my behalf. Long-distance supports received from you have been very important to continue towards the goal. I also like to thank all of my Ecuadorian and international friends who supported me during my stay far away from home.

The current work is financially supported by the Ecuadorian people. Åforsk is gratefully acknowledged for giving me the opportunity to present my work at a conference. Additional support from various projects (Energy Agency) within the department was also received.

List of Publications

This Licentiate thesis is based on the following papers:

I. *Highlights of Fuel Cell Modeling From a Lattice Boltzmann Method Point of View*
M. Espinoza, B. Sundén, and M. Andersson
Proceedings of ASME 2014 International Mechanical Engineering Congress & Exposition IMECE2014, Montreal, Quebec, Canada, November 2014.
doi:10.1115/IMECE2014-37010.

II. *Lattice Boltzmann Modeling From the Macro- to the Microscale - An Approximation to the Porous Media in Fuel Cells -*
M. Espinoza, B. Sundén and M. Andersson
21st Symposium Renewable Energy and Hydrogen Technology Symposium, Stralsund, Germany, November 2014.

III. *Analysis of Porosity and Tortuosity in a 2D Selected Region of Solid Oxide Fuel Cell Cathode Using the Lattice Boltzmann Method*
M. Espinoza, B. Sundén, M. Andersson and J. Yuan
Fuel Cell Seminar & Energy Exposition, Los Angeles CA, USA. November 2014.
Also included in ECS Transactions, Volume 65. 2015. doi: 10.1149/06501.0059ecst, ECS Trans. 2015 volume 65, issue 1, 59-73.

IV. *Compress Effects on Porosity, Gas-phase Tortuosity and Gas Permeability in a Simulated PEM Gas Diffusion Layer*
M. Espinoza, M. Andersson, J. Yuan and B. Sundén
International Journal of Energy Research, 39(11), 1528-1536.

Contents

Abbreviattions and Symbols

Abbreviations

AFC	alkaline fuel cell
BE	Boltzmann equation
BGK	Bhatnagar-Gross-Krook
CL	catalyst layer
DMFC	direct methanol fuel cell
FC	fuel cell
GDL	gas diffusion layer
YSZ	yttria-stabilized zirconia
LBE	lattice Boltzmann equation
LBM	lattice Boltzmann method
LGA	lattice gas automata
LHV	lower heating value
LSM	lanthanum strontium manganite
MC	Monte Carlo
MD	molecular dynamics
MCFC	molten carbonate fuel cell
MEA	membrane electrode assembly
PAFC	phosphoric acid fuel cell
PDF	particle distribution function
PEM	polymer electrolyte membrane
PEFC	polymer electrolyte membrane fuel cell
SEM	scanning electron microscope
SOFC	solid oxide fuel cell
TPB	three phase boundary
UPS	uninterruptible power supply

Symbols

a	constant values in Eq. (10)
C	species concentration
c	velocity vector on lattice
d	diameter of circular obstacle
F_c	force term related to the concentration distribution
F_Q	force term related to the temperature distribution
f	particle distribution function
H	height
L	length
lu	length lattice unit
M	number of lattice nodes in horizontal direction
N	number of lattice nodes in vertical direction
n	position in Eqs. (18) - (20)
Pr	Prandtl number
Q	reaction rate considered in force term, temperature distribution
R	reaction rate considered in force term, mass distribution

Re	Reynolds number
r	position vector
S	source term in Eq. (36)
s	separate region around the circular obstacle
T	temperature field
t	time
ts	time lattice unit
U	absolute velocity in physical problems
u	macroscopic flow velocity from LBM calculations
u_x	horizontal component velocity
w	weighting factor in equilibrium distribution function
y	vertical position Eq. (49)

Greek symbols

α	diffusion parameter in Eqs. (34) - (36)
Δ	change of the variable
γ	aspect ratio
ϑ	solid/pore function
ϕ	scalar variable in equilibrium distribution function
φ	transported variable in Eqs. (33) - (36), porosity Eqs. (54) – (55)
μ	x 10^{-6}
ϱ	fluid density for each lattice node
∇	gradient operator
∇^2	Laplacian operator
τ	relaxation time, tortuosity Eq. (56)
ν	kinematic viscosity
ω	collision frequency
Ω	collision operator

Subscripts

avg	average
entrance	relative to the channel entrance length
gas-phase	relative to the gas-phase
i	relative to the *i-th* variable
i,j	relative to the position in x and y, respectively
in	relative to the entrance, in-flow
LBM	relative to correspondent variables in LBM system
mag	magnitude of a vector
max	relative to the maximum value of the variable
T	relative to the temperature parameters in LBM
x	relative to x- direction
2D	relative to two- dimensional variable

Superscripts

eq	equilibrium

Chemicals

CH_4	methane
CH_3OH	methanol

CO	carbon monoxide
CO_2	carbon dioxide
$CO_3^{=}$	carbonate ion
H_2	hydrogen
H^+	hydrogen ion
H_2O	water
H_3PO_4	phosphoric acid
H_2S	hydrogen sulfide
KOH	potassium hydroxide
$LiAlO_2$	lithium aluminium oxide
Ni	nickel
O_2	oxygen
OH^-	hydroxide ion
$O^{=}$	oxide ion
Pt	platinum
Y_2O_3	yttrium oxide (yttria)
ZrO_2	zirconium dioxide (zirconia)

List of Figures

List of Tables

Chapter 1

1 Introduction

In this chapter an overview of the Licentiate thesis is given. The first part begins with the explanation of the importance of renewable energy in current days, and then the presence of the fuel cells worldwide is detailed. Then research objectives and the methodology applied are presented. Finally, how the information is presented along this document is outlined.

1.1 Research Motivation

The increasing population, energy demand, limited fossil fuel reserves, and related environmental issues are some of the motivations to find alternative and clean sources of energy around the world. There are several discussions about when the oil peak will be reached [1]; followed by continuous decrease of reserves, but there is no discussion that this is really going to happen. While there are discussions about when the oil peak will happen, the energy consumption and extraction of fossil fuels continue to increase in a sustained way [2], and furthermore billions of tons of pollution gases are emitted to the atmosphere resulting in an increase of the global average temperature [3].

To face the afore-mentioned problems, renewable energies appear as a solution for getting energy in an environmentally friendly and clean way, avoiding emissions of pollution gases, due to the no-dependence on fossil fuels during the energy conversion process. Examples of renewable energies include: solar, wind, hydropower, biomass and geothermal. Utilization of these kinds of energy sources has been increasing during the last years around the world [4]. Each one of them has advantages and disadvantages depending on the power scale application, but all of them reach the aims of providing energy in a cleaner way and reduction of pollution gases emitted. Independently which kind of renewable energy one chooses, there is a device that is able to work in direct or indirect form with them because its ability for adapting to different fuels, output power and applications. This device is the fuel cell (FC).

Basically, a FC is an electrochemical device that converts the chemical energy present in the fuel into thermal and electrical energy with outstanding efficiency, especially in relative small systems, and clean manner. They can operate in a wide range of temperatures depending on the electrolyte used, and are able to provide electrical power for different applications nowadays, i.e., portable, transport and stationary systems. According to a Fuel Cell Today report in 2013 [5], during the last years the number of installed units have increased, with a similar effect on the installed power. During the period 2009 – 2013 the increment of installed units is approximately 364 %; whereas that related to the power, in the same period, is around 149 %. Figure 1 shows the mentioned increments considering data from 2009 to 2012, and forecast information for 2013.

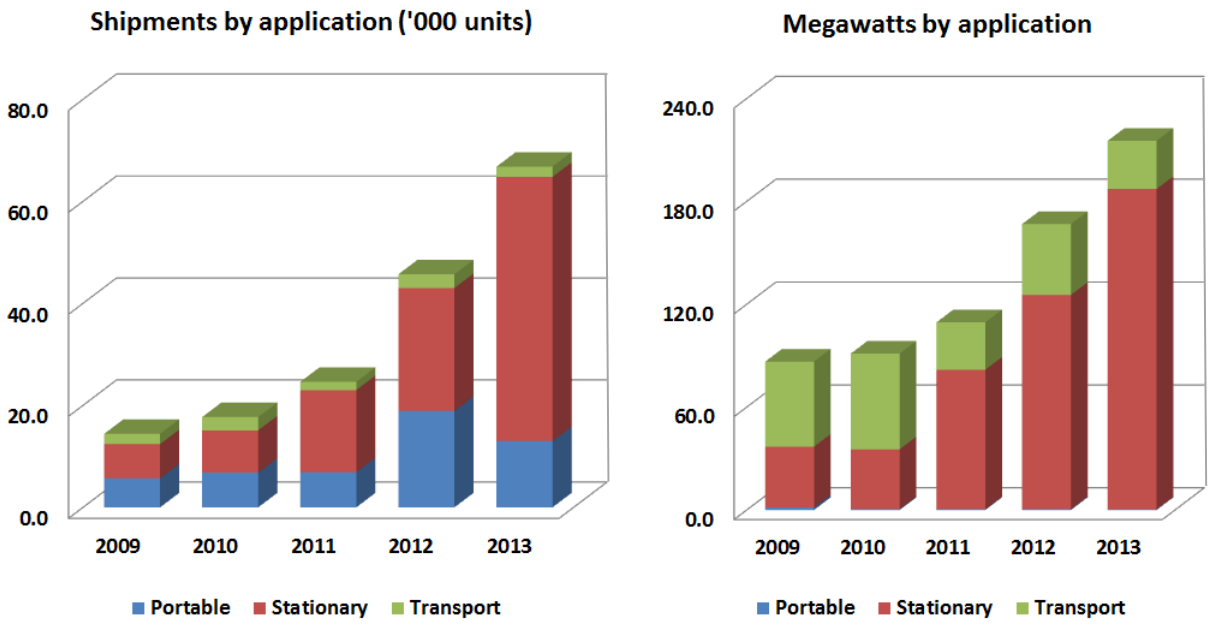

Figure 1. The graph shows the increment of the presence of FCs units and power during the last years. Left, evolution of the FCs installed units around the world during the period 2009-2013. Right, evolution of the FCs power applications worldwide in the same period [5]. Note that data related to 2013 are predicted. This information is found in the "Fuel Cell Industry Review 2013", a report presented by Fuel Cell Today.

Despite the sustained increment of the number of FC systems around the world is clear in Figure 1, as results of environmental motivations, public incentives, and/or improvement of efficiency, the fraction of FCs systems compared with other sources of electrical/thermal energy is still low. This scenario is mainly given for the cost of the different parts of the FC systems as well as their durability. Additionally, as a new technology it needs time to be implemented in the world market.

Understanding in depth the several physical and chemical phenomena that occur inside the FCs can contribute to decrease of the material cost and improvement of the efficiency of the system. Inside FCs, there are several layers that allow the fluids to reach the electrolyte. Once the gases are in contact with the catalyst, the electrochemical reaction takes place; and then electrical energy is produced (more details about the FC energy conversion process will be given in the next chapter). Commonly, because of their characteristics, the material of the mentioned layers are considered as porous media. Knowing the fluid flow behavior in FCs' porous media under different conditions will help to find the best microstructural configuration, allowing an improved efficiency and a reduced material cost.

The microstructural parameters are an important key to describe the FC's behavior. However, various assumptions are commonly considered when studying the FCs at microscale. Considering that the first step in the process for improving the microstructural configuration is modeling the different physical and chemical phenomena at microscale, and adding that modeling is a helpful tool to predict possible scenarios that can occur during the design and fabrication of the new FC systems. The aim of this work is to provide relevant information about the porous media microstructures within FCs. Because of their dominant presence in different applications, i.e., portable, stationary and transport systems, polymer electrolyte membrane fuel cell (PEFC) and solid oxide fuel cell (SOFC) are treated in this work.

To solve the fluid flow in microstructures, the Lattice Boltzmann method (LBM) has proven to be a suitable and efficient microscale methodology. LBM is able to be adapted for different boundary conditions and solve complex geometries. Using LBM, problems that involve advection and advection-diffusion phenomena can be solved, and electrochemical reactions can be included in the model as well. Due to the mentioned characteristics, the simulation results of this work are obtained using LBM. Detailed information about LBM will be given in the corresponding chapter.

1.2 Research Objectives

The main objective of the present work is to gain understanding of the fluid behavior in the porous media present within PEFCs and SOFCs from a microstructural point of view using the LBM. The detailed objectives are mentioned as follows:

- Validate the LBM as a tool for modeling different physical problems for different length scales and Re numbers.
- Make digital reconstructions of different microstructures in porous media at microscale related to FC applications.
- Prove the ability of LBM for solving physical problems in porous media.
- Solve transport phenomena that occur throughout the different porous media layers in FCs.
- Evaluate microscopic parameters in FCs related to the porous media.

1.3 Methodology

The hydrodynamic behavior of LBM is validated before the fluid simulations in porous media of the FCs are conducted. Different physical phenomena are solved, i.e., channel flow, lid-driven cavity and laminar flow around a circular obstacle. The objective is to show the ability of LBM for solving problems at different geometries, and to get a better understanding of the different boundary conditions that can be applied in porous media related problems. All the simulation results presented in this work are based on a 2D model, for the channel flow and flow around a circular obstacle. The velocity fields are determined. In the case of the lid-driven cavity, the momentum equation and the energy equation are modeled. The software employed to implement the various models is MATLAB version R2013a.

Applications of the LBM for solving problems in FC porous media are investigated. The first approximation is an artificial porous media, corresponding to the domain in which solid obstacles are placed in an aleatory way. The second implementation is a digital representation of a selected section of an SOFC cathode. The third example represents the approximation of the gas diffusion layer in a PEFC. In the previously mentioned applications, the velocity field of the fluid is simulated and microstructural parameters are determined, i.e., porosity and tortuosity. In the GDL simulation, also the permeability is calculated.

1.4 Thesis Outline

The overview of the thesis is presented in Chapter 1. In Chapter 2, a general description about FCs is provided, the different types of FCs, and more detailed information about the two kinds of FCs studied are presented. Additionally, a brief explanation about FC modeling and the different transport phenomena that can be modeled are given. Chapter 3 is mainly focused on the description and explanation of LBM, advantages and disadvantages, as well as the methodology applied to solve the problems and main types of boundary conditions implemented. LBM-benchmarking is presented in Chapter 4, and solutions to several physical problems are provided. Chapter 5 presents the simulation results of various microstructures related to porous media in FCs. Finally, the conclusions and future work are outlined in Chapter 6.

Chapter 2

2 Literature Survey and Problem Statement

The present chapter includes a brief description of FCs. Characteristics of the different types of FCs as well as more detailed information about PEFCs and SOFCs are provided. An introduction to FC modeling in porous media and the different governing equations involved in different transport phenomena are presented.

2.1 Introduction to Fuel Cells

A FC is an electrochemical device that converts the chemical energy present in the fuel, i.e., chemical compounds with hydrogen as constitutive element, into electrical/thermal energy and water. This energy conversion is carried out in a clean way, i.e., no pollution gases are emitted when pure hydrogen is used, and considerably reduced amount of pollution when no pure hydrogen is participating. Additionally, the conversion efficiency is higher than in gas turbine and combustion engine systems especially if low power ratings are considered [6], i.e., less than 1 MW.

In general, a single FC is formed by three main components: anode, cathode and electrolyte. The first two are on each side next to their corresponding flow plates, and the electrolyte is between them. Anode and cathode materials have such characteristic that facilitates the fluids, i.e., liquids and gases involved in the energy conversion, to be in contact with the electrolyte. Once the conversion is done, the free electrons can follow the external circuit according to the application. Figure 2 shows a schematic picture of a single fuel cell.

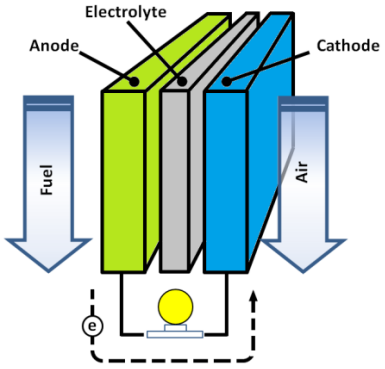

Figure 2. Simplified scheme of a single FC. Simplified representation of the constitutive elements in a single FC. Anode, cathode and electrolyte material compound and characteristics depend on the type of FC.

2.1.1 Types of Fuel Cells

The electrochemical reactions involved during the energy conversion process depend on the type of fuel cell. Considering the constitutive materials of each FC, the efficiency, operating temperature and power output differ, and therefore the applications can vary depending on the mentioned characteristics. FCs can be grouped based on the mentioned variables. However, the most accepted classification is according to the material of the electrolyte. Taking into account the electrolyte type, the most important FCs are:

- Alkaline Fuel Cell (AFC)
- Direct Methanol Fuel Cell (DMFC)
- Molten Carbonate Fuel Cell (MCFC)
- Polymer Electrolyte Membrane Fuel Cell (PEFC)
- Phosphoric Acid Fuel Cell (PAFC)
- Solid Oxide Fuel Cell (SOFC)

Table 1 is an adaptation from [7], and shows the different characteristics of the mentioned FC types. The variables considered are electrolyte, working temperature, efficiency, applications among others. More detailed information about the FCs in which this work is focused, i.e., PEFCs and SOFCs, is given in the following sub-chapters.

Table 1. General overview of FC characteristics. Different FCs and their characteristics are presented in this table. Note that the capacity in the table corresponds to the electrical power considering for single cell/stack applications.

Parameters	***Fuel cell types***					
	AFC	***DMFC***	***MCFC***	***PEFC***	***PAFC***	***SOFC***
Electrolyte	Liquid solution of KOH	Solid polymer membrane	Lithium and potassium carbonate ($LiAlO_2$)	Solid polymer membrane (Nafion)	Phosphoric acid (H_3PO_4)	Stabilized solid oxide electrolyte (Y_2O_3, ZrO_2)
Operating temperature (°C)	50 - 200	60 - 200	~ 650	50 - 100	~ 200	600 - 1000
Charge carrier	OH^-	H^+	$CO_3^=$	H^+	H^+	$O^=$
Fuel	Pure H_2	CH_3OH	H_2, CO, CH_4, other hydrocarbons	Pure H_2	Pure H_2	H_2, CO, CH_4, other hydrocarbons
Oxidant	O_2 in air	O_2 in air	O_2 in air	O_2 in air	O_2 in air	O_2 in air
Efficiency (%) (LHV)	~ 50	40	> 50	40 - 50	40	> 50
Capacity (kW)	10 - 100	0.001 - 1000	155 - 2000	0.03 - 250	100 - 1300	1 - 1700
Applications	Transportation; space shuttles; portable power	It is used to recharge batteries in mobiles; computers and other portable devices	Transportations (e.g. marine-ships; naval vessels; rail); industries; utility power plants	Residential; UPS; emergency (hospitals, banking, industry) transportation; commercial	Transportation; commercial cogeneration; portable power	Residential; utility power plants; commercial cogeneration; portable power

2.1.2 Polymer Electrolyte Membrane Fuel Cells (PEFCs)

The PEFC is an electrochemical device that converts the energy present in the fuel, i.e., pure hydrogen, into the electrical energy and water. The operating temperature of the PEFCs is in the range of 50 – 100 °C, and some of their advantages are: high power density, a quick start-up, and a solid non-corrosive electrolyte.

To facilitate the energy conversion, PEFCs are built with several parts in form of layers. These layers allow the flow of the fluids that participate in the process, except the electrolyte. The electrolyte is the central part, called polymer electrolyte membrane (PEM), and allows only the flow of hydrogen ions (H^+). On both sides of the membrane, a catalyst layer (CL) is placed, and together with these the gas diffusion layers (GDL) are arranged to facilitate the gas distribution. All these layers together form the so-called membrane electrode assembly (MEA). Figure 3 shows the schematic of a single PEFC.

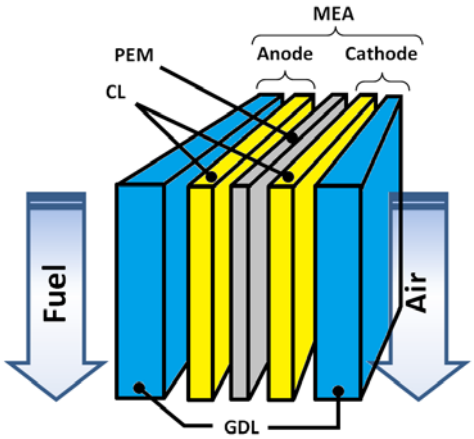

Figure 3. Basic structure of a single PEFC. Simplified representation of the constitutive elements in a single PEFC. Note that the thickness of the layers is not to scale.

Fuel used in a PEFC must be pure hydrogen, which flows at the anode side and is distributed by the GDL. The electrochemical reaction is occurring within the CL, the hydrogen ions pass through the electrolyte and as result the free electrons can follow the external circuit. On the cathode side, the hydrogen ions reacts with oxygen molecules and electrons, and gas-phase water molecules are formed. The electrochemical reactions involved in the energy conversion process are simplified as:

$$Anode\ Reaction: H_2 \rightarrow 2H^+ + 2e^- \quad (1)$$

$$Cathode\ Reaction: \frac{1}{2}O_2 + 2H^+ + 2e^- \rightarrow H_2O \quad (2)$$

Examples of PEFCs disadvantages are the high cost of the catalyst material included in the CLs, i.e., platinum, and its sensitivity to fuel impurities (CO, H_2S). Thermal balance is an important issue to take into account because a membrane being too dry/wet influences the PEFC performance.

2.1.3 Solid Oxide Fuel Cells (SOFCs)

Similar to the PEFC, the SOFC is an electrochemical device that converts the chemical energy present in the fuel into electrical/thermal energy and steam. The main difference is that pure hydrogen is not required as fuel. Due to the high temperature operation (600 – 1000 °C), different reforming reactions can be performed which allows fuel flexibility. Solid electrolyte, and high electrical conversion efficiency are considered as its advantages. Additionally, a high amount of heat generated can be used for co-generation in power systems.

If other fuel different to hydrogen is used, a reforming process is performed. Hydrogen molecules obtained after the reforming process diffuse through the anode and combine with oxygen anions ($O^{=}$), that come from the cathode passing through the solid electrolyte, producing water. Free electrons on the anode side are conducted by an external circuit to the cathode. Commonly, the SOFC is constructed with different layers, but it differs from PEFCs that the layers are not totally independent/separated. Support layers, active layers and electrolyte are the constitutive elements in the SOFCs. The schematic of a single SOFC is shown in figure 4.

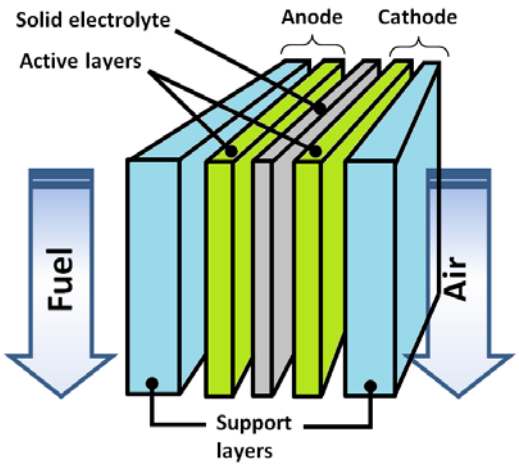

Figure 4. Basic structure of a single SOFC. Simplified representation of the constitutive elements in a single SOFC. Note that the thickness of the layers is not to scale.

There is no explicit separation between the different layers, and the most common SOFC type is the anode-supported one which implies a thicker region of the anode side. In this FC type, the water is produced at the anode side. The simplified electrochemical reactions involved in the conversion process are as follows:

$$Anode\ Reaction: H_2 + O^{=} \rightarrow H_2O + 2e^{-} \tag{3}$$

$$Cathode\ Reaction: \frac{1}{2}O_2 + 2e^{-} \rightarrow O^{=} \tag{4}$$

Some disadvantages in SOFCs that can be mentioned are: high cost and intolerance to sulfur. Considering that a high temperature is required, a slow start-up makes the SOFCs not the best candidate for supplying energy in portable or transportation markets.

2.2 Porous media in SOFCs and PEFCs

In FCs, the multifunctional layers between the channels and electrolyte must allow for the flow of the different reactants/products involved in the electrochemical process. In PEM- and SOFCs, the fuel has to be in contact with the so-called three phase boundary (TPB) so that the electrochemical reactions can be performed. Therefore, these layers should be made of porous materials. It is important to notice that the electrolyte only allows the flow of the charge carrier, and an absolutely impermeable material is required.

Fundamentally, the layers of an SOFC are constructed with yttria-stabilized zirconia (YSZ) because it has good behavior at high temperatures, i.e., no considerable physical deformation, good ionic and electronic transport. Depending on the side designed, the other composites are nickel (Ni) and lanthanum strontium manganite (LSM) for the anode and cathode respectively. In the PEFC case, the GDL is constructed with carbon fiber papers, whereas the CL is made of carbon agglomerates with encrusted particles of platinum (Pt). To observe the microstructural architecture of these layers, Figure 5 is presented.

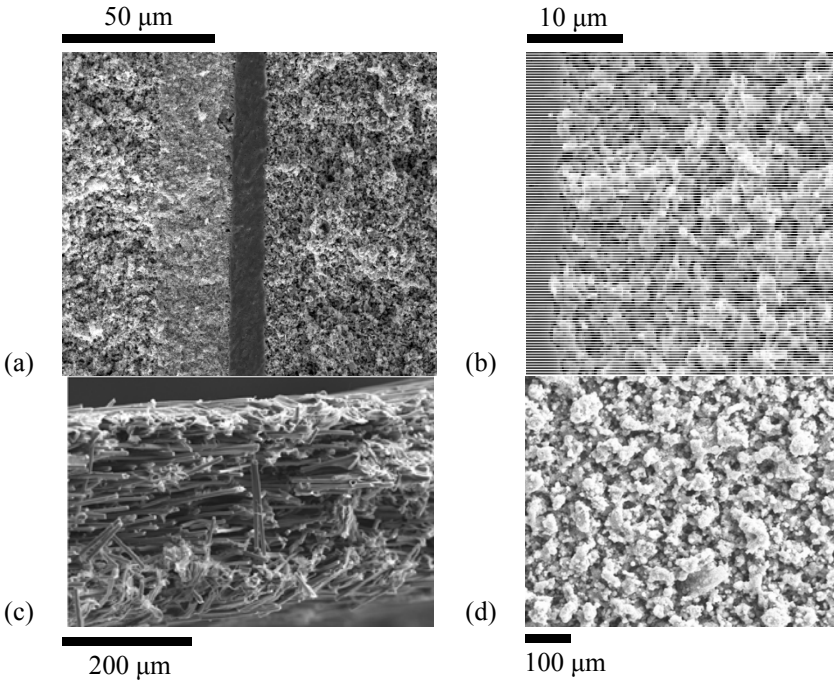

Figure 5. Scanning electron microscopic (SEM) image of SOFC and PEFC layers. (a) Surface image of SOFC anode, electrolyte and cathode. The darkest part corresponds to the electrolyte. (b) Approaching image of the SOFC electrolyte and cathode. Thanks to NIMTE for SOFC images. (c) Cross section view of a characteristic GDL [8], image presented with permission of the author. (d) Surface image of CL [9].

The microstructural characteristics showed in Fig. 5 facilitate the flow of reactants to allow an appropriate energy conversion in the FCs. Porosity, the measure of the void spaces in a material and determined as the ratio between the void volume and total volume, has different values for each of these layers. In different studies, the pore-size is the other variable considered to describe the morphological layer characteristics. Details about porosity values, pore-size, and layer thickness are presented in Table 2. Note that the values are only such found in the literature.

Table 2. Characteristics of the different layers in FCs. Some values of thickness, porosity and pore-size are given as example in this table. The applicable values are not restricted to the presented. Values obtained from [10 – 17].

FC types	*FC part*	*Thickness (μm)*	*Porosity (%)*	*Pore-size (μm)*
PEFC	Gas diffusion layer	200 – 500	70 – 80	20 – 30
	Catalyst layer	9 – 34	51 – 61	0.05 – 0.1
SOFC	Active layer	10 – 60	20 – 50	0.2 – 10
	Support Layer	600 – 1500	30 – 56	0.3 – 1

Taking into account the microstructural parameters is important to improve the FC efficiency. This can be achieved by finding alternative microstructural configurations to reduce material costs and increase electrical efficiency. The behavior of the fluids through these layers, i.e., CL, GDL, anode and cathode, can be modeled at meso- and microscale. Validation versus experimental data of the different microstructural shapes or compounds is important.

2.3 Fuel Cell Modeling

To date, a complete three dimensional FC model with detailed physical and chemical phenomena is still a pending task. Such a task is considerably more difficult if different scales are considered simultaneously, i.e., length scales and time scales. Additionally, the coupling between the different scales is a topic that has to be studied to obtain such a complete FC model.

To solve different chemical and physical phenomena, suitable length and time scales are required. Having chosen length and time scales, another variable to take into account is the computational cost. Different techniques to reduce the computational cost during the modeling process have been implemented during the last years, e.g., parallel computing. This is supported by the increase of the available computational power. A simple scheme showing the relationship between the computational cost, time- and length scales is provided in Figure 6, adapted from [18].

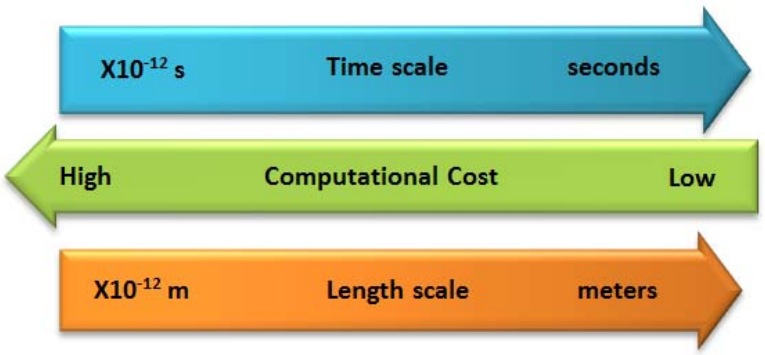

Figure 6. Symbolic representation of the length scale, time scale and computational cost. Note that the computational cost is higher when phenomena at small scales are modeled.

There is no specific methodology for solving the different transport phenomena at the selected scale. To solve problems related to homogeneous transport phenomena, i.e., momentum, mass, charge and heat transfer, which occur between the nanoseconds to minutes (time scale) and between the nanometers to meters (length scale), different methods such as discrete element and phase field methods, lattice Boltzmann method, finite volume and finite difference method can be applied [19]. Considering the mentioned length and time scales, the methods applied can be grouped in molecular dynamics (MD), Monte Carlo (MC), and continuum [20].

According to [18], micro- and mesoscales correspond to the lengths between the nanometer and hundreds of micrometer; and taking into account the given characteristics of the porous media presents in FCs in Table 2, LBM appears as an advisable tool for modeling the transport phenomena in the porous media.

In the current work, to study the transport phenomena that occur within the porous media in FCs and to recover the microscopic behavior of the fluids, the LBM is applied. Modeling the different transport phenomena at micro- and mesoscale will give useful information for improving the microstructural architecture of the FCs, and to find alternative materials with the aim to increase the efficiency and reduce cost. LBM, main characteristics, and governing equations are given in more details in the following chapter.

Chapter 3

3 Lattice Boltzmann Method – LBM

In this chapter detailed information about LBM, advantages, governing equations, boundary conditions and methodology for solving the different transport phenomena equations in porous media related to FCs are given. The information given in this chapter is mainly based on Paper I.

3.1 Introduction to LBM

Although LBM is considered as a powerful tool to solve problems at micro- and mesoscale [21 - 23] in applied porous media of FCs, several previous studies have demonstrated that it can also solve physical problems at macroscale [24, 25]. The interest for using this methodology is because it can handle pore-level phenomena in complex structures, i.e., porous media and moving boundaries with considerable accuracy. Additionally, the local solution allows the algorithm to be implemented using parallel computing, and hence the computational time is decreased. As a result, the number of publications related to LBM in different research fields has been increasing during the last years [18].

LBM originates from lattice gas automata (LGA). For solving the properties of one entity, it considers the properties of their neighborhoods. However, LGA presents several disadvantages as mentioned in [23], and hence LBM has gained space in the modeling field.

The first step, when applying LBM in a physical problem, is to divide the domain into small entities called lattice nodes. Each lattice node has its own properties and these are linked with their neighborhoods by the velocity connections. Based on this information, the scheme in LBM is defined. The common way to represent the lattice scheme is to define the dimension of the problem to be solved, i.e., one-, two- or three-dimensional, and the number of linked velocities involved in the solution. The scheme representation is given as follows:

$$DnQm \tag{5}$$

where n represents the dimension of the problem to be solved, and m is related to the number of linked velocities between the lattice nodes. For instance, the scheme D1Q3 is used to solve a one-dimensional problem; and in this case, each lattice node has two linked velocities with its neighborhood. The most common schemes applied in LBM are D2Q9 and D3Q19, and these are shown in Figure 7.

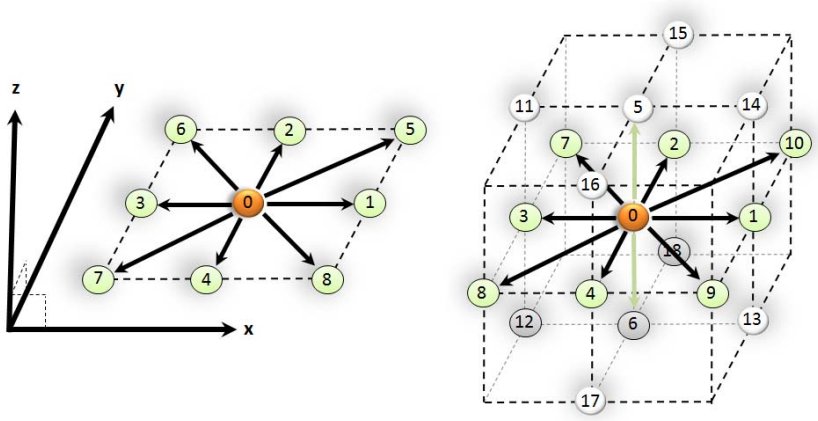

Figure 7. Most common lattice schemes applied to solve problems using LBM. D2Q9 (left) and D3Q19 (right). Orange node is the central node, and the others are the neighboring nodes.

The properties of each lattice node, small spheres in Figure 7, are represented for the particle distribution function (PDF). This function is equivalent to the number of particles of the fluid in a determined region within a range of velocities at a certain time. The connections of each lattice node with its neighbors depend on the scheme used, and each connection has a different weight factor. More details about the weight factors are given in the next subchapter.

3.2 LBM Governing Equation

The backbone of lattice Boltzmann models is the Boltzmann equation (BE), which depends on the PDF. In general, the BE is an integral-differential equation and to solve it is cumbersome. BE can be expressed as follows:

$$\frac{\partial f(r,t)}{\partial t} + c \cdot \nabla f(r,t) = \Omega \tag{6}$$

where f is the particle distribution function, r the position vector, t the time, and c the velocity vector. Ω is the so-called collision operator and depends on f. Therefore, the collision operator is described as function of the position and time.

As mentioned above, solving Eq. 6 is complicated because of the position and velocity dependence of the collision operator (Ω). In 1954, Bhatnagar, Gross and Krook, proposed a simplified model to determine this operator. Nowadays, this approximation is widely used and expressed as follows [26]:

$$\Omega = \omega[f^{eq} - f] = \frac{1}{\tau}[f^{eq} - f] \tag{7}$$

where ω is the collision frequency, an important variable for modeling the different transport phenomena. τ is the relaxation time, and f^{eq} the equilibrium distribution function.

Equation (7) is the so-called BGK approximation, and represents the fact that the collision tends to relax to an equilibrium value. Using Eqs. (6) - (7), and taking into account the vectorial characteristic of the variables, the lattice Boltzmann equation (LBE) is obtained:

$$\frac{\partial f_i(r,t)}{\partial t} + c_i \, \nabla f_i(r,t) = \frac{1}{\tau}\left[f_i^{eq}(r,t) - f_i(r,t)\right] \tag{8}$$

In the above equation, the equilibrium distribution function (f^{eq}) and the relaxation time (τ) should be defined according to the transport phenomena to be solved. Equation (8) can be expressed in a discretized manner as follows:

$$f_i(r + c_i \, \Delta t, t + \Delta t) = f_i(r,t) + \frac{\Delta t}{\tau}\left[f_i^{eq}(r,t) - f_i(r,t)\right] \tag{9}$$

The main issue of Eq. (9) is to determine the equilibrium distribution function. Depending on the physical/chemical problem to be solved, this function behaves in different manner. In general, the equilibrium distribution function is determined as [27]:

$$f_i^{eq} = \phi \, w_i \, [a_1 + a_2 \, c_i \cdot u + a_3 \, (c_i \cdot u)^2 + a_4 \, u^2] \tag{10}$$

where Φ is a scalar parameter related to density, temperature or species concentrations, u is the macroscopic velocity vector, w_i is the weighting factor, and a_1, a_2, a_3 and a_4 have to be defined based on the conservation equation applicable, i.e., mass, momentum and energy. More detailed information about these values (a_1, a_2, a_3 and a_4) is given in Sub-chapter 3.4.

Weighting factor (w_i) and velocity (c_i), will take values depending on the number of linked velocities between the lattice nodes; and as mentioned, the number of linked velocities depends on the scheme utilized in the model. Table 3 presents the corresponding values according to the applied scheme.

Table 3. Weighting factors for the most common LBM schemes. The highest value of weight is assigned to the central node, and it decreases according to the distance to its neighbor direction. The sum of all values is always unity. Table is adapted from [28].

	Linked direction	w_i	c_s
D2Q9	$i = 0$	$4/9$	$\frac{1}{\sqrt{3}}$
	$i = 1 - 4$	$1/9$	
	$i = 5 - 8$	$1/36$	
D3Q19	$i = 0$	$1/3$	
	$i = 1 - 6$	$1/18$	
	$i = 7 - 18$	$1/36$	

Once Eq. (8) is solved, it is possible to recover the macroscopic variables implied in the problem using the following relations:

$$\rho(r,t) = \sum_i f_i(r,t) \tag{11}$$

$$\rho(r,t)\ u(r,t) = \sum_i c_i\, f_i(r,t) \tag{12}$$

where ρ is the fluid density of each lattice node, and u is the macroscopic flow velocity.

3.3 Solving Algorithm

To solve physical/chemical problems with LBM, various steps in a defined sequence have to be followed. Based on the problem, the equilibrium distribution function has to be defined for each lattice node. How to calculate the equilibrium distribution function is explained later.

After the equilibrium distribution function is calculated, the collision distribution of particles for all lattice nodes is determined. This calculation is done using Eq. (9). Once the collision step is applied, the streaming is implemented, and finally the macroscopic variables can be calculated in each time step. To precise the solution algorithm, Figure 8 is presented.

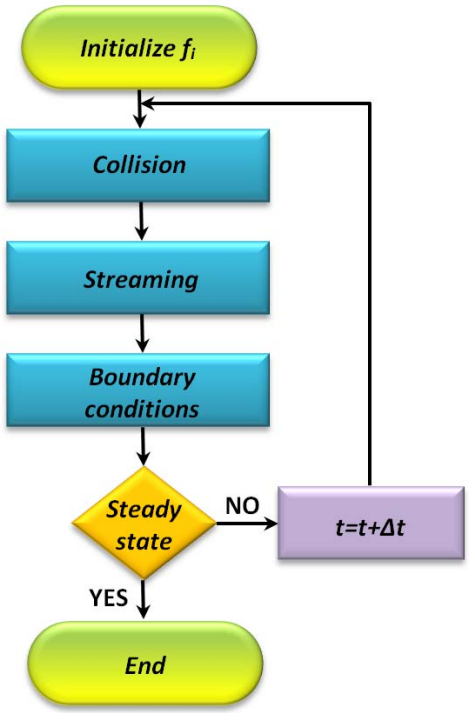

Figure 8. Main steps followed during LBM implementation. To know if the steady state is reached, the macroscopic variables are computed. If steady state is not reached, the steps are repeated and the particle distribution functions are updated. Boundary conditions are crucial in the implementation process, and will be explained in the next sub-chapter.

3.4 Boundary Conditions

An important issue to be explained before solving physical/chemical problems using the LBM is the treatment of the boundary conditions. In the following sub-chapters the expressions to be applied in lattice Boltzmann models are presented, but complete demonstrations are avoided. Boundary conditions are obtained by applying mass and momentum conservation at the boundaries. Readers wishing more detailed information related to the demonstrations of boundary conditions are referred to [29 - 31]. Because the simulations presented in this work are developed in 2D, the description of the boundary conditions are based on the D2Q9 scheme.

3.4.1 In/Out Flow Boundary Conditions

To specify which PDFs are considered as unknown after the streaming process, Fig. 9 is showed. This figure presents the known and unknown variables after streaming for the right side boundary. The same treatment can be applied for each side of the domain.

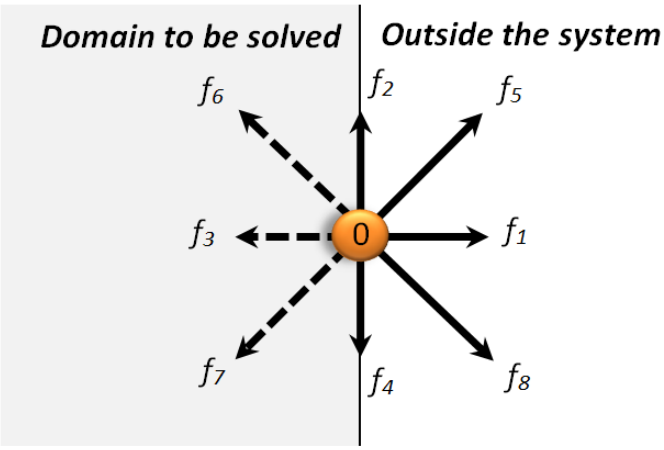

Figure 9. Scheme to identify the PDFs unknown in the right side boundary of the domain. After streaming, PDFs which come from inside the domain are known (f_1, f_2, f_3, f_5 and f_8), and represented by solid arrows. Unknown PDFs come from outside the system (f_3, f_6 and f_7) and are presented by dashed arrows.

Depending on the flow model, the boundary conditions implemented are based on either the velocity or the pressure. If the boundary is defined by the velocity, it is referred to as von Neumann (Flux) Boundaries. On the other hand, when the pressure is given, they are referred to as Dirichlet (Pressure) boundaries [30].

Velocity Boundary

To implement a velocity boundary, the velocity is a known characteristic. Based on Figure 9, the particle distribution to be determined is represented by f_3, f_6 and f_7. Applying the mass and momentum conservation, calculating ϱ using the given velocity u_x and the particle distribution functions known, the group of equations to handle this boundary is expressed as follows:

$$\rho = \frac{1}{1+u_x}\,[f_0 + f_2 + f_4 + 2(f_1 + f_5 + f_8)] \tag{13}$$

$$f_3 = f_1 - \frac{2}{3}\,\rho\,u_x \tag{14}$$

$$f_6 = f_8 - \frac{1}{6}\,\rho\,u_x + \frac{1}{2}\,(f_4 - f_2) \tag{15}$$

$$f_7 = f_5 - \frac{1}{6}\,\rho\,u_x + \frac{1}{2}\,(f_2 - f_4) \tag{16}$$

Pressure Boundary

When the pressure is given, the so-called Dirichlet boundary has to be implemented. Following the previous description and considering the unknown particle distributions from Figure 9, the equations for implementing this boundary correspond to the last three equations with the difference that u_x is unknown, and therefore must be determined before calculating the unknown particle distributions.

The solution for u_x from Eq. (13), can be expressed as follows:

$$u_x = \frac{1}{\rho}\,[f_0 + f_2 + f_4 + 2(f_1 + f_5 + f_8)] - 1 \tag{17}$$

Once the velocity is known the unknown particle distributions, i.e., f_3, f_6 and f_7 can be calculated using Eqs. (14) – (16).

To determine the boundary conditions for the other sides, i.e., up, bottom, and left side, the process to follow is the same as for both velocity and pressure boundaries.

Second derivative approximation

When neither the velocity nor the pressure are known, the particle distribution function in the outlet can be determined using a second derivative approximation. Although in this implementation the locality of LBM is not considered, it represents a useful alternative for solving the unknown PDFs. The implementation is as follows according to [27]:

$$f_{3,n} = 2\,f_{3,n-1} - f_{3,n-2} \tag{18}$$

$$f_{6,n} = 2\,f_{6,n-1} - f_{6,n-2} \tag{19}$$

$$f_{7,n} = 2\,f_{7,n-1} - f_{7,n-2} \tag{20}$$

where n represents the position of the particle distribution to be calculated, i.e., right side boundary, while *n-1* and *n-2* are the two previous consecutive positions.

3.4.2 Bounce-back Boundary Conditions

The bounce-back boundary condition plays an important role when transport phenomena in porous media are modeled. The difference between solid and fluid particles is established, and no treatment in solid nodes is required. If after the streaming one fluid node is going to collide with one solid node, e.g., part of the wall, bounce-back conditions have to be implemented. Basically, the fluid particles are reflected in the same action line from which they came but in opposite direction.

Based on Figure 9, considering the domain to be solved as the fluid part and the outside of the system region as the solid part, the bounce-back implementation is as follows:

$$f_3 = f_1 \tag{21}$$

$$f_6 = f_8 \tag{22}$$

$$f_7 = f_5 \tag{23}$$

where f_1, f_8 and f_5 are known from the streaming process.

3.4.3 Periodic Boundary Conditions

Figure 10 illustrates the scheme for the application of periodic boundary conditions. The region between the red dotted lines corresponds to the domain to be solved. The unknown particle distributions are represented by doted arrows, and are defined as function of the PDFs crossing the boundary lines.

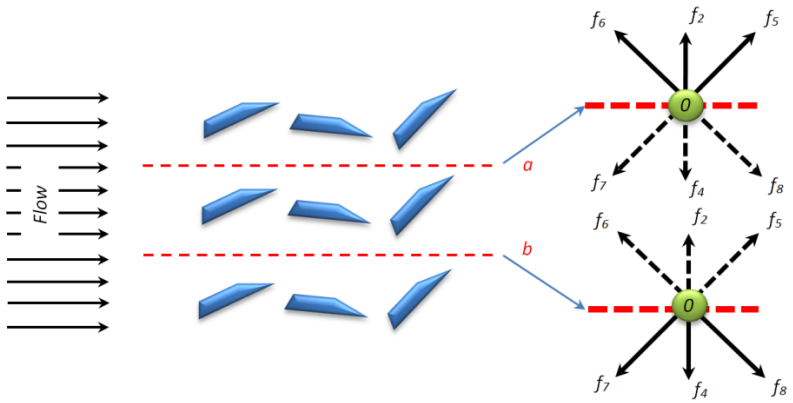

Figure 10. Scheme to identify the unknown PDFs for periodic boundary implementation. After streaming, PDFs which come from inside the domain are known and represented by solid arrows. Unknown PDFs come from outside the system and are presented by dashed arrows.

The distribution functions f_4, f_7 and f_8 are unknown on line *a*, and f_2, f_5 and f_6 are unknown on line *b*. Periodic boundary conditions are implemented as follows:

$$f_{4,a} = f_{4,b} \tag{24}$$

$$f_{7,a} = f_{7,b} \tag{25}$$

$$f_{8,a} = f_{8,b} \tag{26}$$

along line *a*, whereas along line *b* the conditions are implemented by:

$$f_{2,b} = f_{2,a} \tag{27}$$

$$f_{5,b} = f_{5,a} \tag{28}$$

$$f_{6,b} = f_{6,a} \tag{29}$$

3.4.4 Symmetry Boundary Conditions

Symmetry boundary conditions are helpful to reduce computational cost when physical and chemical phenomena are modeled. Although heterogeneity of the porous media does not allow one to use symmetry conditions, application in macroscopic problems where symmetry appears is recommended.

An example where the symmetry conditions can be applied is the flow in a channel. In this situation, the solution of the complete number of lattice nodes is not required. The domain is divided into two half-domains and only the half of the lattice nodes are solved. Under these circumstances, the symmetry line is defined and the following conditions are applied:

$$f_4 = f_2 \tag{30}$$

$$f_7 = f_6 \tag{31}$$

$$f_8 = f_5 \tag{32}$$

where f_4, f_7 and f_8 are the unknown particle distributions in the half-domain to be solved, illustrated in Fig. 11.

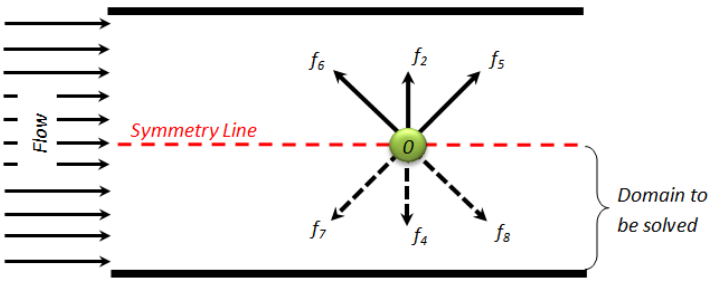

Figure 11. Scheme to identify the PDFs unknown for symmetry boundary implementation. Half-domain, i.e., the bottom side, is solved using the known PDFs using Eqs. (30) – (32) along the symmetry line.

3.5 Transport Phenomena

The aim of this part is to give detailed information about the different transport phenomena that occur within the porous media at microscale inside FCs. To solve these transport phenomena, the LBM is applied and some relevant characteristics in implementing this methodology are explained in this sub-chapter.

Before starting with the description of LBM solution for the different transport phenomena, equations to model these phenomena are presented, from the most simple to the complex, i.e., advection, diffusion, advection-diffusion, and advection-diffusion including a source term.

When the advection phenomenon is analyzed, the transport of the variable to be studied occurs due to the bulk velocity of the fluid. In general, the advection equation can be expressed as:

$$\frac{d\varphi}{dt} + (u \cdot \nabla)\varphi = 0 \tag{33}$$

where φ is the variable transported, u the velocity vector, t the time, and ∇ the gradient operator.

In the pure diffusion phenomenon, no velocity of the fluid is considered. However, the diffusion parameters of the variable is included in Eq. (34).The diffusion equation is expressed as:

$$\frac{d\varphi}{dt} = \alpha\, \nabla^2\varphi \tag{34}$$

where ∇^2 is the Laplacian operator, and a is the diffusion parameter. Depending on the variable transported; the diffusion parameter is established. If momentum, mass or energy diffusion is analyzed, a is replaced by the kinematic viscosity, mass diffusion coefficient, and thermal diffusivity, respectively.

When the advection-diffusion phenomenon occurs, the variable is not only transported but also diffused. The expression to represent the advection-diffusion problem is as follows:

$$\frac{d\varphi}{dt} + (u \cdot \nabla)\varphi = \alpha\, \nabla^2\varphi \tag{35}$$

which is a combination of the two previous equations.

Finally, if the advection-diffusion phenomenon is carried out in the presence of electrochemical reactions or a source S, which depends on the variable transported or electrochemical reactions involved, an extra term is added to Eq. (35) as follows:

$$\frac{d\varphi}{dt} + (u \cdot \nabla)\varphi = \alpha\, \nabla^2\varphi + S \tag{36}$$

3.5.1 Momentum Transport

From the characteristics of LBM, the solution of momentum transport is explained in detail. The solutions for other transport phenomena are similar. For the momentum transport there is only one PDF because the fluid is treated as a gas mixture, whereas for mass transport the number of PDFs depends on the number of species analyzed [32].

As mentioned earlier in this chapter, the LBE is the backbone of the methodology, and the BGK approximation gives us an appropriate solution for the selected transport phenomena based on the equilibrium distribution function, which will establish the variable studied.

The equilibrium particle distribution function for momentum transport is defined as [30]:

$$f_i^{eq}(r) = w_i \ \rho(r) \left[1 + 3\frac{c_i \cdot u}{c^2} + \frac{9}{2}\frac{(c_i \cdot u)^2}{c^4} - \frac{3}{2}\frac{u^2}{c^2}\right] \tag{37}$$

where r is the position of the corresponding lattice node, w_i and c_i are defined in Table 3, c is the basic speed on the lattice.

Once the collision, streaming and treatment of the boundary conditions are carried out. As mentioned in Figure 8, recovering the macroscopic velocity field is given as:

$$u = \frac{1}{\rho}\sum_i c_i \, f_i \tag{38}$$

3.5.2 Mass Transport

For modeling mass transport in LBM, the advection-diffusion equation is solved. The equilibrium particle distribution function does not take into account the four terms as for the momentum transport. According to [30], the equilibrium particle distribution is expressed as:

$$f_i^{eq}(r) = w_i \ C(r) \left[1 + 3\frac{c_i \cdot u}{c^2}\right] \tag{39}$$

where C is the concentration at each position, and is calculated in a similar manner as the fluid density:

$$C = \sum_i f_i \tag{40}$$

Depending on the number of species, the number of particle distributions and their corresponding equilibrium particle distributions must be defined. More detailed information can be found in [33].

3.5.3 Electrochemical Reactions

When the gases diffuse through the porous media in FCs and reach the reaction sites, the chemical reactions can be included in the model by adding the force term in the local distribution function [34]. The local distribution function plus the force term is expressed as:

$$f_i(r + c_i\,\Delta t, t + \Delta t) = f_i(r,t) + \frac{\Delta t}{\tau}\left[f_i^{eq}(r,t) - f_i(r,t)\right] + F_c \tag{41}$$

where F_c depends on the reaction rate of the chemical reaction involved, and can be calculated as:

$$F_c = \sum_i w_i\ \Delta t\ R \tag{42}$$

where Δt is the time step defined on the lattice, and R the reaction rate. For more detailed information about the reaction rate definition, the reader is referred to [35].

3.5.4 Energy Transport

The temperature distribution follows similar procedure as the mass transport, therefore Eqs. (39) and (40) are used to determine the particle distribution function and field temperature, respectively. In both equations, concentration C is replaced by a temperature field T.

If heat is generated due to the electrochemical reactions, a source term should be added in the local distribution function. It can be added as follows [36, 37]:

$$f_i(r + c_i\,\Delta t, t + \Delta t) = f_i(r,t) + \frac{\Delta t}{\tau}\left[f_i^{eq}(r,t) - f_i(r,t)\right] + F_Q \tag{43}$$

where F_Q represents the force term (source term) that considers the heat generated by electrochemical reactions. The force term (source term) is defined as:

$$F_Q = \sum_i w_i\,\Delta t\ Q \tag{44}$$

where Δt is the time step defined on the lattice, and Q is the heat generated. The heat generated is determined as the heat generated by the electrochemical reactions minus the heat generation due to the activation, ohmic and concentration polarizations as mentioned in [20, 38, 39].

Chapter 4

4 LBM – Benchmarking

To demonstrate LBMs ability to solve different problems, the solution and validation for channel flow, lid-driven cavity and flow over a circular cylinder are presented in this chapter. The domain studied is for the 2D case in all examples. The scheme D2Q9 is used and the results are compared with previous studies. To explain the relation between the variables in the physical system and the LBM system, details about the relation between these are given in the first example. The information presented in this chapter is mainly based on Paper II.

4.1 Developing flow in a 2D Channel

The first example to validate the LBM is the channel flow. By obtaining the velocity profile at different positions along the flow direction, the entrance length can be determined and the fluid behavior explained.

Water is going from the left to the right side between the two parallel plates as shown in Figure 12. The entrance velocity is considered equal to 1 cm/s, the distance between the plates is 2 cm, and the plate length is 80 cm.

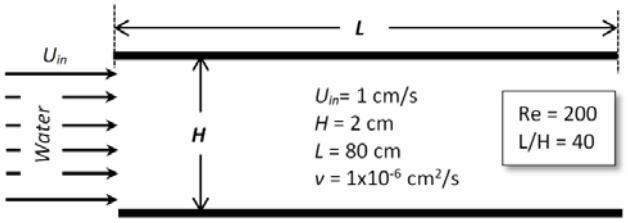

Figure 12. Physical characteristics of the 2D channel. Velocity field is solved using LBM. The real problem and LBM equivalent system is solved matching certain values, for this case Re and the aspect ratio are considered.

To solve the problem using LBM, non-dimensional characteristics are considered and they are matched to the LBM system. The kinematic viscosity of water is set to 1x10^{-6} m^2/s, the Reynolds number of the physical system is determined by the definition:

$$\mathrm{Re} = \frac{U_{in}\,H}{\nu} = \frac{(0.01)(0.02)}{1x10^{-6}} = 200 \tag{45}$$

Another characteristic to take into account is the aspect ratio, which is defined according to the size of the domain as follows:

$$\gamma = aspect\ ratio = \frac{L}{H} = \frac{80\ cm}{2\ cm} = 40 \tag{46}$$

Using Re and γ, the LBM variables are defined. Re in LBM can be expressed as:

$$\mathrm{Re}_{LBM} = \frac{U_{LBM}\, N}{\nu_{LBM}} \tag{47}$$

where U_{LBM} and ν_{LBM} are the inlet velocity and kinematic viscosity in LBM system, respectively. N is equal to the number of lattice nodes that will be used in the vertical direction.

The values of U_{LBM} and N can be selected arbitrary but Re_{LBM} must match with Re. If U_{LBM} is 0.1 lu/ts and N is equal to 35 lu, then the kinematic viscosity in LBM can be calculated using Eq. (47), and the number of lattice nodes in the x- direction is determined using the aspect ratio. As a result, ν_{LBM} = 0.0175 lu^2/ts and M = 1400 lu.

To solve the momentum equation in the channel, the relaxation time is defined as a function of the kinematic viscosity in the lattice system. Based on the scheme applied, the relation between these two variables is as follows [30]:

$$\nu_{LBM} = \frac{1}{3}\left(\tau - \frac{1}{2}\right) \tag{48}$$

From Eq. (48) the relaxation time is 0.553 ts, and therefore the collision frequency ω is 1.810 ts^{-1}. Using the variables in the LBM system and following the methodology explained in the previous chapter, the velocity field is calculated.

Figure 13 shows the equivalent problem expressed in LBM units.

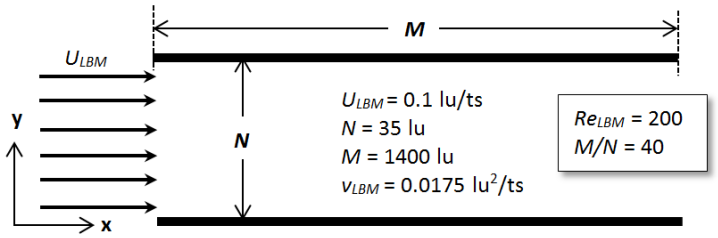

Figure 13. Equivalent LBM system for the 2D channel. The variables can be selected in order to match the variables of the real system. There are restrictions with the U_{LBM} velocity, for instance higher velocities can produce instability in the solution.

The solved domain corresponds to 49000 lu^2, i.e., 1400 lu in the x-direction and 35 lu in the y-direction. Bottom and top boundaries are treated with the bounce-back boundary condition, whereas for the inlet a von Neumann boundary is implemented because the velocity is given. The outlet boundary is solved with the second derivative approximation.

Figure 14 shows the velocity distribution calculated using the LBM. A red color represents higher velocity values and a blue color lower velocities. To observe the velocity field, the aspect ratio is not considered in the figure, i.e., the length and height are not to scale.

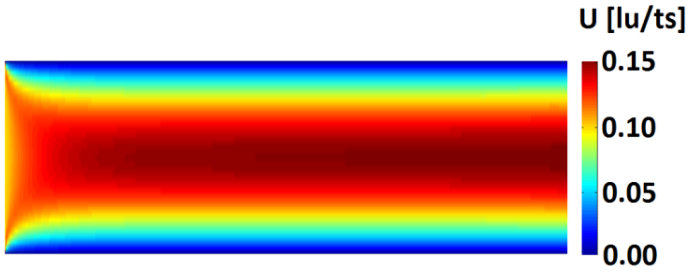

Figure 14. Velocity field solution for the 2D channel using LBM. This figure shows the velocity field distribution in the solved domain. Higher velocities are given in red color and lower velocities in blue color.

To validate the LBM solution, the velocity profile at different x-positions are shown in Figure 15 together with the analytical solution of the fully developed velocity profile, which is given by [40]:

$$u = u_{max}\left[1 - \left(\frac{y}{H}\right)^2\right] \tag{49}$$

where u_{max} is the maximum velocity at the center of the channel, commonly defined as 1.5 times the average velocity [27], and y is the vertical position where the velocity is measured.

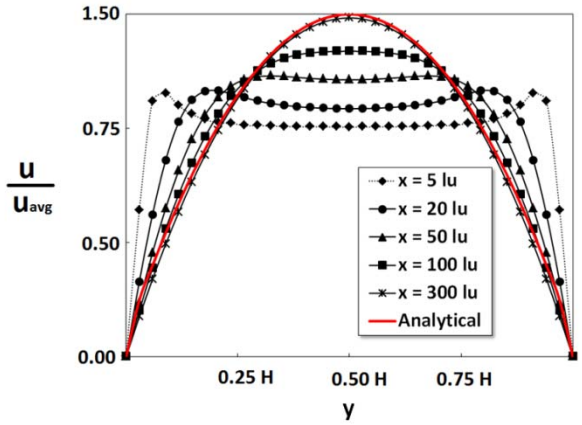

Figure 15. Velocity profiles for 2D channel. Velocity profiles at different x-positions are given. The profile presented in red color corresponds to the analytical solution of the velocity profile for the fully developed region. This profile is reached at x = 306 lu according to the LBM solution.

According to the numerical results by LBM; the entrance length, i.e., the distance from the entrance where the velocity at the center line reaches 99 % of the velocity for fully developed flow [41], occurs at the position x = 306 lu. If this value is compared with the one calculated using the proposed equation in [42]:

$$\frac{L_{entrance}}{H} = [(0.631)^{1.6} + (0.0442\ Re)^{1.6}]^{\frac{1}{1.6}} \tag{50}$$

the deviation error is around 3.0 %, which is reasonably accurate.

4.2 Lid-Driven Cavity

A lid-driven cavity has been widely investigated as a benchmark problem. The velocity field for isothermal fluid and the energy distribution for non-isothermal fluid are presented in this sub-chapter. Simulation results obtained in this work are compared and contrasted with previous studies.

4.2.1 Velocity Field

In the case of an iso-thermal fluid the variables taken into account are the same as in the previous example, i.e., the Reynolds number and the aspect ratio.

A fluid filling a square cavity is considered, and the lid velocity is given on the top. Physical characteristics of the problem are given in Figure 16. Following the explained methodology for the previous example, these physical characteristics must match with the LBM system.

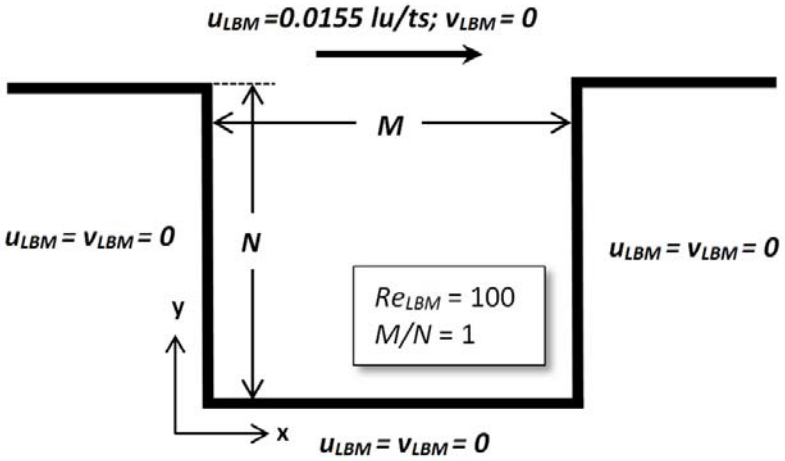

Figure 16. LBM characteristics for solving the velocity field of an isothermal fluid in a square cavity. The number of lattice nodes in x- and y-directions are chosen according to the Reynolds number and aspect ratio from the real problem. As in the real problem, velocity values at the walls are established as zero for LBM system whereas at the top the velocity is maximum.

The boundary condition implemented at the top is a von Neumann boundary because the velocity is known. On the walls, bounce-back boundary conditions are applied. As expected, the LBM simulation shows that the lid velocity produces the main rotation of the fluid in the clock-wise direction as is shown in Figure 17.

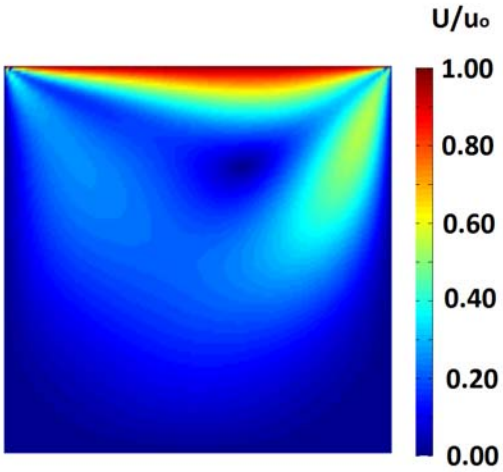

Figure 17. Simulation results of the velocity field of an isothermal fluid in a square cavity. The clock-wise circulation can be appreciated in the figure. Higher velocities are represented in red color, and lower velocities in blue color.

To validate the results shown in Figure 17, obtained using the LBM, two imaginary lines are traced in the cavity. One vertical line at the middle of the domain along the x- direction (mid plane), and one horizontal line at the half-height of the vertical direction. Velocity values are taken at selected points to compare with the work done by Ghia et al. [43]. Figure 18 shows the result in the mentioned work by a continued line and the results obtained in the present work by red dots.

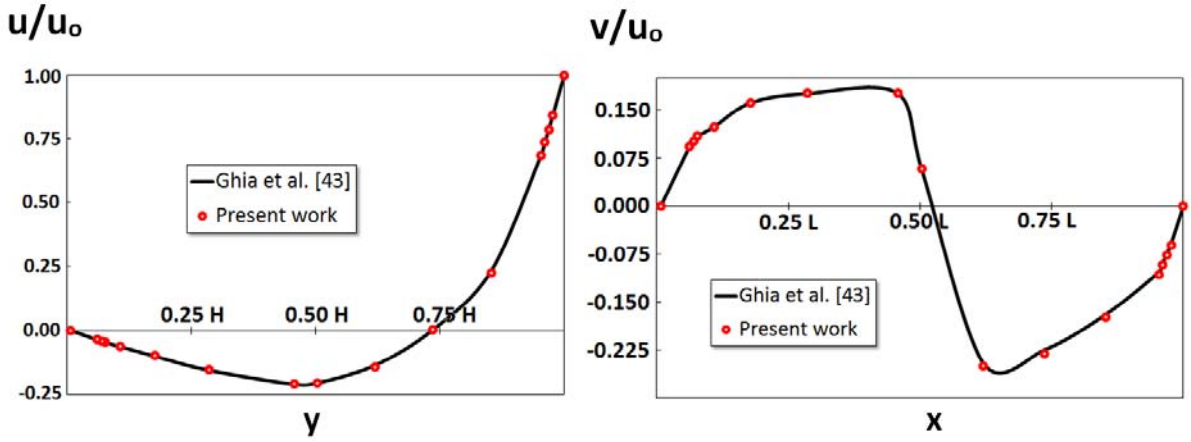

Figure 18. Validation of velocity field results using LBM of an isothermal fluid in a square cavity. Horizontal and vertical velocities taken from different points in the domain solved using LBM are compared with the results from the work done by Ghia et al. This is one of the most widely used studies to validate the velocity field results in cavity phenomena.

The comparison between this work and the work found in the literature shows a good agreement in the velocity values. The results in this work differ from the referred results up to 3.91 % and 3.57 % for horizontal and vertical velocities, respectively. This shows that the accuracy of LBM is reasonable.

4.2.2 Temperature Field

To apply the LBM in the solution of the energy equation, the heated lid-driven cavity is solved, and the results are validated. The steps for solving the energy equation are similar to the momentum equation with the following changes: a new PDF is defined to calculate the temperature field in each lattice node, the equilibrium particle distribution for this new variable take the form of an advection-diffusion problem, and the Prandtl number (Pr) is used to determine the relaxation parameter in the temperature solution.

The problem is defined using Re = 1000 and the domain size is represented by a square. The cavity is filled with air, and the lid is heated to a high temperature. The temperature at the vertical walls is set at lower temperatures, and the bottom is considered thermally insulated. Considering normalized temperatures the top is established at 1.0 and the vertical walls at 0.0. The equivalent system in LBM is represented in Figure 19.

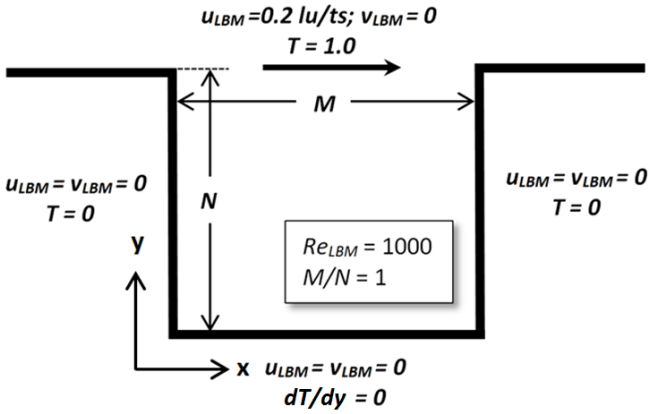

Figure 19. LBM characteristics for solving the temperature field of a non-isothermal fluid in a square cavity. The number of lattice nodes in x- and y-directions are chosen according to the Reynolds number and aspect ratio from the real problem. Prandtl number allows to determine the relaxation parameter for the new equilibrium PDF.

Because this problem corresponds to the solution of a non-isothermal fluid, the relaxation parameter for the equilibrium particle distribution function for the temperature must be defined. This can be done using the Prandtl number (Pr) definition, and matching these physical characteristics with the variables in the LBM system as follows:

$$\Pr = \frac{\nu}{\alpha} = \frac{\nu_{LBM}}{\alpha_{LBM}} \tag{50}$$

where ν is the kinematic viscosity, and α is the thermal diffusivity of the fluid.

At normal conditions, Pr for air is approximately equal to 0.71. Setting the kinematic viscosity in LBM system equal to 0.02 lu^2/ts and using Eq. (50), the thermal diffusivity value in LBM system is 0.028 lu^2/ts. Once the thermal diffusivity in LBM is determined, it is possible to calculate the relaxation time using the following equation [27]:

$$\alpha_{LBM} = \frac{1}{3}\left(\tau_T - \frac{1}{2}\right) \tag{51}$$

Solving the last equation for the relaxation time gives 0.585 ts, and the collision frequency ω_T is 1.711 ts^{-1}. Following the methodology detailed in previous chapter the temperature field is calculated. Figure 20 shows the temperature field for the heated lid-driven cavity under the mentioned characteristics.

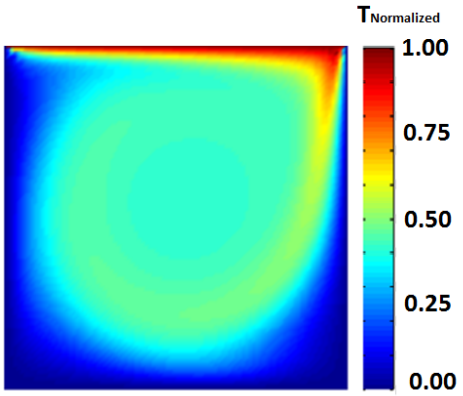

Figure 20. Simulation results of the temperature field of a non-isothermal fluid in a square cavity. Higher temperature is at the top, and the distribution in the picture shows relation with the velocity behavior.

To validate the temperature field obtained by LBM, three different cross sections were selected: at the first quarter, middle and third quarter planes. These results are shown in Fig. 21 (right), and compared with the results found in [27].

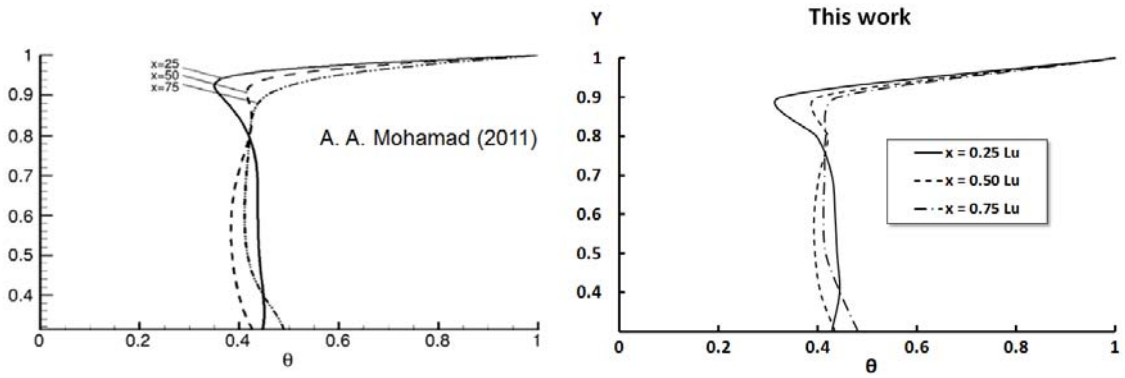

Figure 21. Validation of the temperature field found using LBM in a heated lid-driven cavity. Three different cross sections were selected at x = 25 lu, x = 50 lu, and x = 75 lu. Cavity represented with 100 lu by side.

4.3 Flow Around a Circular Obstacle

The last example presented as a benchmark is the laminar flow behavior over a circular cylinder. Momentum transport equation is solved for three different Re, and these results are compared with previous studies.

Basically, the domain solved corresponds to a rectangular domain with a circular obstacle in the midline. The circular obstacle has to be placed at a considerable distance from the entrance of the fluid, i.e., 500 lu for the constructed domain. The characteristics of the domain solved are shown in Figure 22.

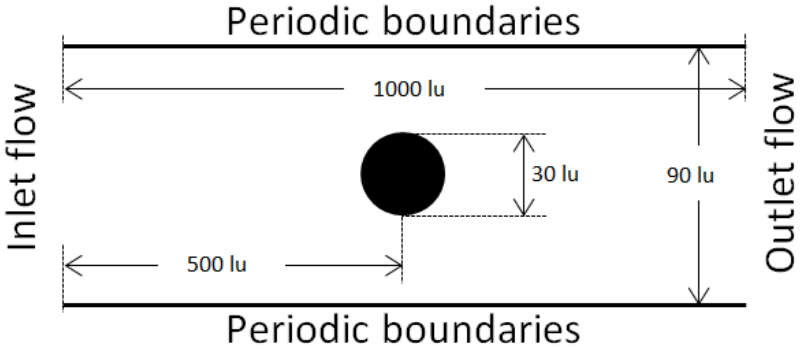

Figure 22. LBM scheme for solving the velocity field flow around a circular obstacle. Inlet is implemented using given velocity, and outlet boundary using pressure. Top and bottom boundaries are considered periodic. Distance from the entrance to the obstacle are to be determined in order to avoid incidence in the flow around the obstacle.

The model allows us to test the fluid behavior for different Re. Varying the velocity at the entrance, three different Re are tested. The velocity fields obtained using LBM are shown in Figure 23. Note that only the closest region around the circular obstacles are presented.

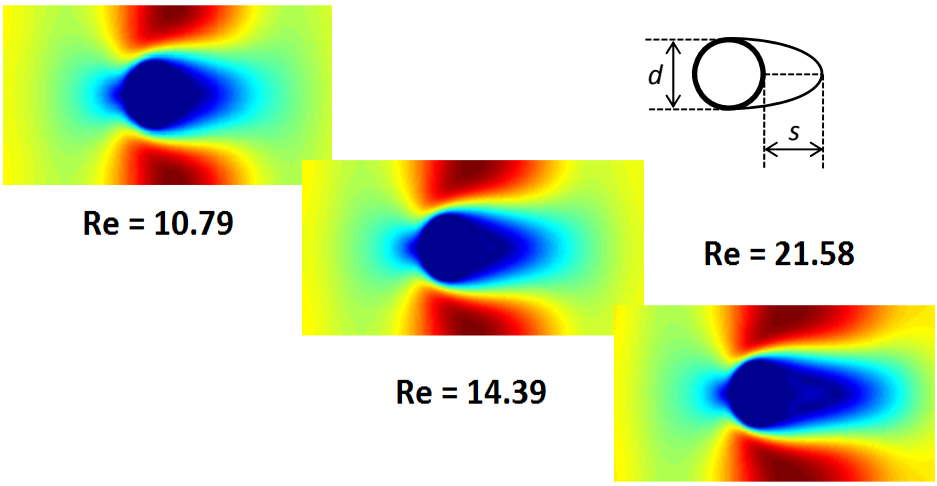

Figure 23. Velocity fields for each Re showing the separate region. When Re increases the separated region (s) increases. Higher velocity regions are represented by red colors, and lower velocities are represented by blue color.

To validate the results obtained using LBM, the ratio between the diameter and the length of the separated region is defined (s/d). Once this ratio is defined and calculated for each Re, they are compared with the relationship obtained from the literature [44]. This relationship can be expressed as follows:

$$\left(\frac{s}{d}\right) = 0.0632\,\mathrm{Re} - 0.3580 \tag{52}$$

where s is the length of the separated region behind the circular obstacle, d the diameter of the circular obstacle, and Re values are determined using the diameter as characteristic length.

The results of this work and the relationship expressed in Eq. (52) are presented in Figure 24. The comparison shows accurate results when LBM is applied for solving the fluid behavior around obstacles.

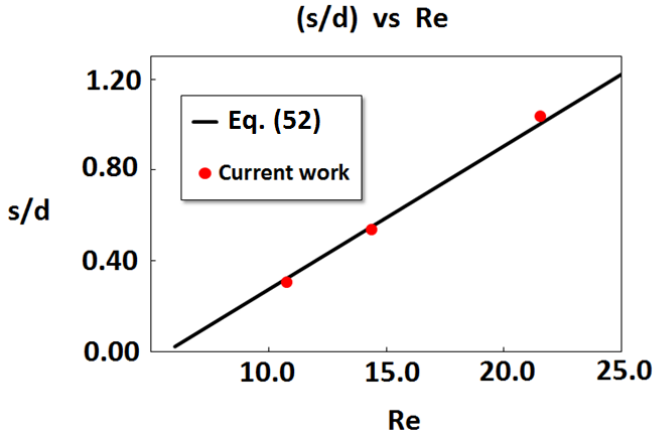

Figure 24. Comparison between relationship found using [44] and results of the current work. The present work is represented by red dots while the previous relationship with the straight line. The error deviation is considerably low, and falls in acceptable values.

The deviation errors fall in the range between 2.73 % and 7.39 %; and therefore, once again LBM has proven to be a powerful tool for handling fluids around solid obstacles with relatively high accuracy in the low Re regime.

In this chapter, different physical problems have been solved using the LBM. The accuracy have been demonstrated with comparison of the current work with previous studies. Different boundary conditions were implemented, and the knowledge acquired in the current chapter is applied in the simulations in the following chapter where the LBM is used to analyze the behavior of fluids in porous media.

Chapter 5

5 Simulations in Fuel Cell Porous Media Using LBM

As mentioned in Chapter 2, porous media are present in different layers of FCs: CL and GDL in PEFCs, and anode and cathode in SOFCs. In this chapter, the fluid flow behavior in different porous media is presented. Microstructural variables such as: porosity, tortuosity and permeability are calculated. The information presented in this chapter is mainly based on Paper III and Paper IV.

5.1 First Approximation to the Porous Media

Before the results are presented, information related to the implementation of the models are given in this paragraph. In porous media there are two parts exactly defined: the pore space and the solid. The image can be constructed from either a real microstructure or an artificially generated microstructure. In both cases, solid obstacles are considered impermeable to the surrounding fluid. A more realistic reconstructed image can be obtained if more lattice units are used. Because it is a porous medium, Re varies throughout the modeling domain. For FC's applications Re ~ 10^{-2} - 10^{-4} can be considered [32, 45].

Considering the artificially generated porous material presented in Figure 25. Solid circular obstacles of different diameters are placed in an aleatory way over the rectangular domain. The number of lattice nodes is defined as a part of the reconstruction image.

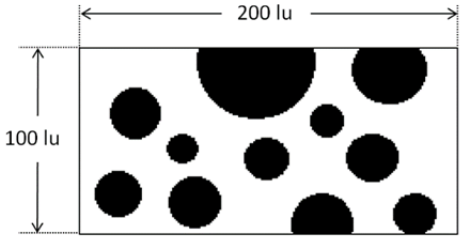

Figure 25. Artificially generated porous material. Particle size is variable throughout the domain. White color corresponds to the void space, and black color is the solid material. Best definition of the solid surface can be obtained using a higher number of lattice nodes. Aspect ratio is 2:1.

For this model, 100 lu and 200 lu were used in the y- and x- directions, respectively. Pore spaces are established in the way that each pore is covered by several lattice nodes according to the suggestions in [46] in order to get an accurate hydraulic behavior.

Solid obstacles can represent YSZ materials in SOFCs, or fiber carbon materials in PEFCs depending on the analysis that is carried out. To translate this image to language understandable for the computer, the BOUND function used in the coding simulations is defined:

$$\vartheta(r) = \begin{cases} 0, & r \,\epsilon\, pore, white \\ 1, & r \,\epsilon\, solid, black \end{cases} \tag{53}$$

In porous media, the porosity is the characteristic property that allows the fluid to pass through the material. Porosity is determined as the ratio between the void space and the total volume occupied by the material, and can be expressed as:

$$\varphi = \frac{Void\ space}{Total\ volume} = \frac{Void\ space}{Void\ space + Solid\ volume} \tag{54}$$

This property is dimensionless, and always between zero and unity. For porosity values in FCs, please refer to Table 2 in Chapter 2. This work presents results of different problems in 2D, i.e., the porosity is calculated as follows:

$$\varphi_{2D} = \frac{Void\ area}{Total\ area} = \frac{Void\ area}{Void\ area + Solid\ area} \tag{55}$$

with the same characteristics of the volumetric definition given after Eq. (54).

Another important parameter for characterization of fluid flow through porous media is the tortuosity. It is commonly treated as a fitting property [20], but using this methodology the exact tortuosity value can be determined depending on the microstructure analyzed. There are different kinds of tortuosity, but in this work the gas phase tortuosity is calculated. Tortuosity is defined as the ratio between the actual path followed for the fluid and the shortest distance that the fluid can take, and is calculated using the following expression [47]:

$$\tau_{gas-phase} = \frac{Actual\ path}{Shortest\ distance} = \frac{\sum_{i,j} u_{mag}(i,j)}{\sum_{i,j} |u_x(i,j)|} \tag{56}$$

where $u_{mag}(i,j)$ is the magnitude of the velocity vector at the position (i,j).

Tortuosity is a dimensionless value, and is always bigger than or equal to unity. The tortuosity plays an important role for the calculation of diffusion parameters as mentioned in [48], which presents a relationship between the diffusion parameter, porosity and the tortuosity.

LBM is applied to solve the velocity field through the artificially generated porous domain presented in Fig. 25, and the previously defined parameters are calculated, i.e., porosity and tortuosity. Solid obstacles are considered impermeable, and bounce-back boundary conditions are implemented. Top and bottom boundaries conditions are considered to be periodic.

The solution of the velocity field is shown in Figure 26. The velocities are normalized with respect to the highest velocity found in the solution. High velocities are represented in red color and low velocities in blue color.

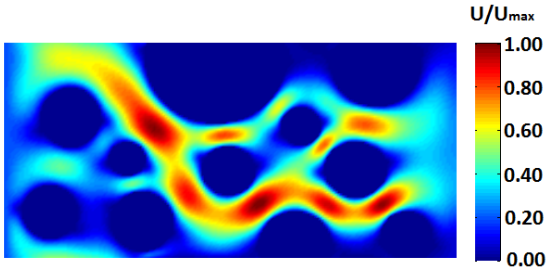

Figure 26. Velocity field solution over an artificially generated porous material. Higher velocities are represented by red color, and lower velocities by blue color. Where the solid material is placed the velocity is zero. Aspect ratio is 2:1.

To find the steady state solution the number of iterations is defined. If steady state is not reached the tortuosity value is not correctly determined. Using Eqs. (55) and (56), porosity and tortuosity values are calculated, and are equal to 0.6432 and 1.2087, respectively.

The tortuosity value obtained in this model was calculated using Eq. (56) after the momentum equation was solved using the LBM. The result obtained in this work agrees well with the expected values presented in [47].

5.2 Flow Simulation in an SOFC Cathode

As mentioned in Chapter 2, different layers of FCs are built as porous media. In this sub-chapter, the analysis of porosity and tortuosity for a 2D case in a selected region of an SOFC cathode is presented. More detailed information about this study can be found in [49].

Because the aim of this work is to study the fluid behavior in microstructures, the selected region corresponds to a square with 10 μm side. The domain solved, i.e., the solid material and the pore space, is digitally recovered from a scanning electron microscope (SEM) image of a real SOFC cathode. Figure 27 shows the microstructure of a section of the SOFC cathode from which the region is selected.

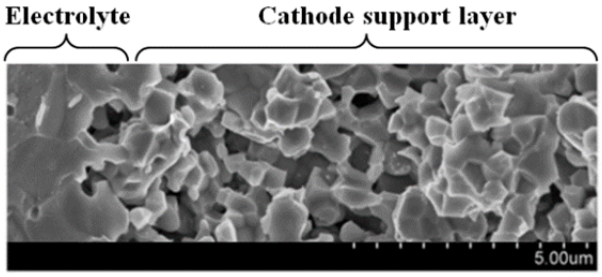

Figure 27. SEM micrograph showing the porous structure of an SOFC cathode. Credits: Ningbo Institute of Materials Technology & Engineering (NIMTE).

The first step to obtain the velocity field through the porous media is to convert the SEM image into a black and white color image. This binary image represents the functional matrix to the model in order to recognize if the lattice node corresponds to solid material or pore space according to Eq. (52). Figure 28 shows the binary image and the selected region (red square) where the velocity field is determined.

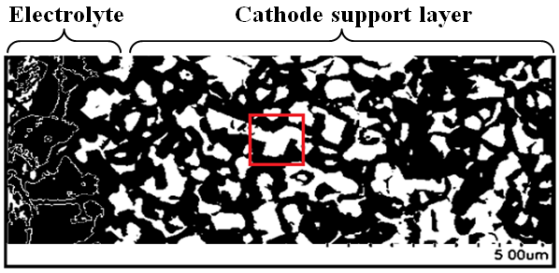

Figure 28. Binary color image for the SOFC cathode. The figure represents the black and white image to recover the solid and pore space in a digital matrix to implement the boundary conditions. (Saturation at 50 %, white color - pore space, black color – solid material).

The fluid is assumed to move from the left to the right, and the bounce-back boundary conditions are applied on the lattice nodes where the solid material is found. To solve the momentum equation, the LBM is applied. The velocity field is shown in Figure 29, and the porosity and tortuosity in the selected region are calculated.

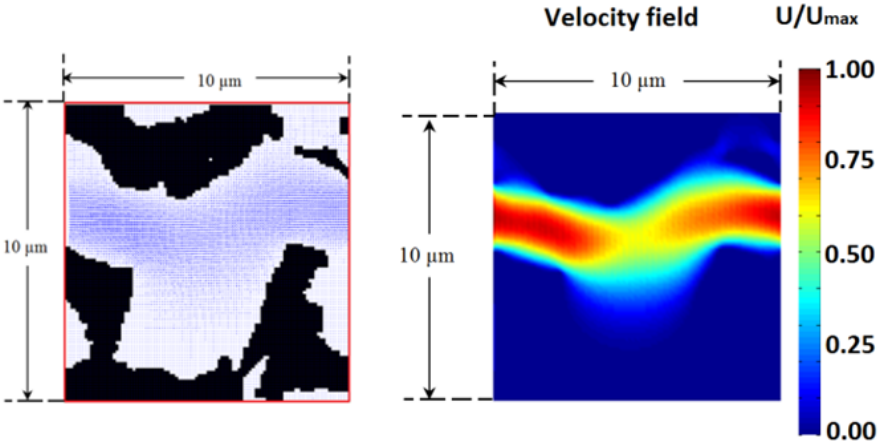

Figure 29. Magnification of the selected region of an SOFC cathode. (left) Velocity field represented by blue arrows. (right) Velocity field for each lattice node; red color represents high velocities, and blue color low velocities. All velocities are normalized with respect to the maximum velocity found.

The porosity of the selected region was calculated digitally using Eq. (55), and is equal to 0.59. The velocity field found allows calculation of the tortuosity value for the selected region. Using Eq. (56), the tortuosity value is 1.18. To evaluate the results obtained in this simulation, they are compared with some porosity-tortuosity relationships from previous studies. This comparison is presented in Table 3. The first column presents four relationships found in the literature, the second column shows the tortuosity calculated using the corresponding relationship and the

porosity found in this work. The last column shows the deviation error between the tortuosity calculated using the mentioned relationships, and the tortuosity value calculated in the current simulation.

Table 4. Comparison of porosity-tortuosity values found in previous studies. Four different porosity-tortuosity relationships are presented to compare the results obtained in this work. To calculate the tortuosity values using the mentioned relationships, the porosity value is required. The porosity replaced in the equations is determined from the reconstructed image. The tortuosity in this model is calculated with the velocity field result after the momentum equation is solved using LBM.

(a) Tortuosity-porosity relationships	***(b) Porosity from this model***	***(c) Tortuosity calculated using (a) and (b)***	***(d) Tortuosity from this model***	***Deviation error between (c) and (d)***
[47] $\tau = -0.5191\varphi^3 + 0.879\varphi^2 - 1.1657\varphi + 1.8058$	0.59	1.32	1.18	10.2 %
[50] $\tau = 0.8(1-\varphi) + 1$		1.33		11.0 %
[51] $\tau = 1 + 0.19\frac{(1-\varphi)}{(\varphi-0.33)^{0.65}}$		1.19		0.4 %
[52] $\tau = 1 - 0.49\,Ln(\varphi)$		1.26		5.7 %

Considering the results in Table 4, the comparison between the previous results and this study gives a deviation less than 11.0 %. The closest value is obtained with the relationship proposed by Koponen et al. [51], with a percentage deviation less than 1.0 %.

5.3 Flow Simulation in a PEFC Gas Diffusion Layer

An important issue during the assembling of the PEFC is the compression the GDLs is subjected to. This compression, which occurs at cell level, influences over the microstructural configuration of the layers; and therefore, the microstructure variables such as porosity, tortuosity and permeability experience changes. Permeability represents the quantification of the ability of fluids to flow through porous media.

By analyzing the GDL compression in detail, it is possible to notice that the layer is not uniformly compressed. This deformation occurs because the contact between the GDL and the flow plate depends on the configuration of the flow plate channels.

In this work, a part of the cross section of the GDL with no compression and subjected to the assembly compression is studied. The model is developed as a two-dimensional case, and the momentum equation for both cases, i.e., normal condition and compressed condition, is solved using the LBM. The fluid behavior in both cases is presented, and the influences of the compression over the microscopic variables are determined by calculating the variables in the initial and final conditions. Figure 30 shows the selected part of the GDL to be modeled for analyzing the mentioned variables, and their changes under compression.

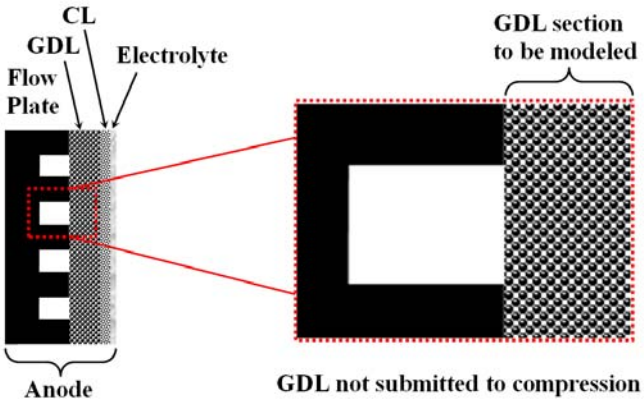

Figure 30. Anode PEFC component layers. (left) Cross sectional view of the different constitutive layers of the anode side of a PEFC. (right) Amplification image showing the selected GDL region to be studied in both conditions, i.e., normal thickness and under compression.

Based on previous studies related to GDLs [53 - 56], the domain size is established and the cross section domain is generated. Taking into account the SEM image of a real GDL and the characteristic porosity value found in the literature, solid obstacles representing the fiber carbons are placed in the domain. The dimensions and characteristics of the digitally created GDL are given in Figure 31. The initial shape and initial fiber positions in the modeled domain are presented.

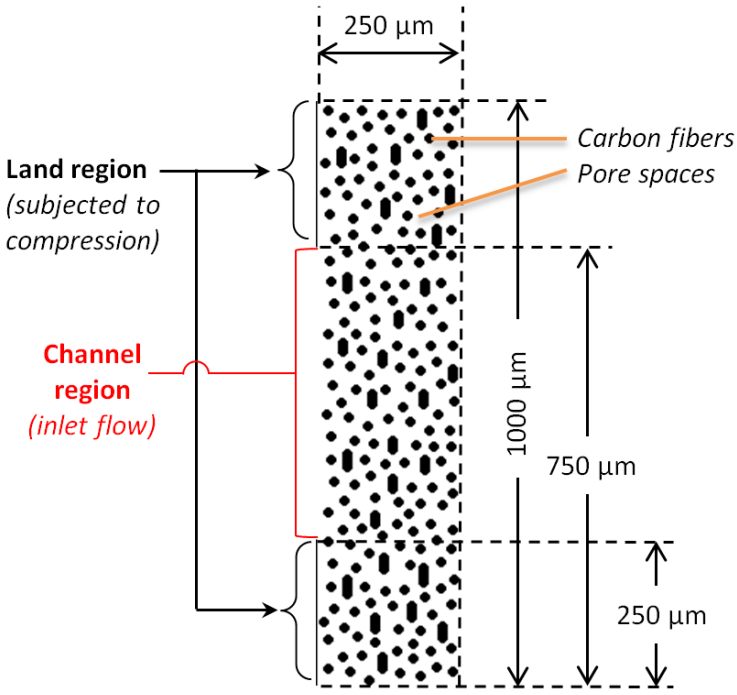

Figure 31. Implemented domain to model a 2D PEFC GDL. The domain is represented by a rectangle of 1 mm and 0.25 mm in y- and x- directions, respectively. The solid obstacles (black) represent the cross sectional view of the carbon fibers. White color represents the pore space between the carbon fibers.

In the model, the porosity and fiber thickness values are considered by taking into account the values found in the literature (porosity = 0.7759, fiber thickness = 7.5 μm). Land region, i.e., the surface that is in contact with the ribs of the flow plates, and the channel region are clearly defined. The position of the fibers is randomly defined.

The fluid moves from the left to the right, and the simulation results are obtained for two different conditions: the first one is without compression, and the second simulation is carried out when the thickness decreases approximately 20% compared to the initial state. The compression is carried out only over the land region; and therefore, there is no significant variation of the fiber positions in the channel region. The compression is given digitally, the fibers placed in the land region are approached mainly with a tendency to the right. The deformation is assumed only in the horizontal direction (through-plane), and because the compression is reflected by the reduction of pore spaces, the fiber thickness is assumed constant between the initial and final stage. The compression rate of the GDL presented in this work is considered reasonable according to the experimental work presented in [57].

The porous domain was built using 400 lu and 100 lu in the y- and x directions, respectively. LBM is applied to solve the velocity field throughout the porous domain when the GDL is not compressed; followed by this calculation, the digital compression is carried out and the velocity field in the compressed GDL is determined. In both cases, the porosity, gas-phase tortuosity and permeability are calculated in order to find the impact of the compression. Figure 32 shows the velocity field when the steady state condition is reached.

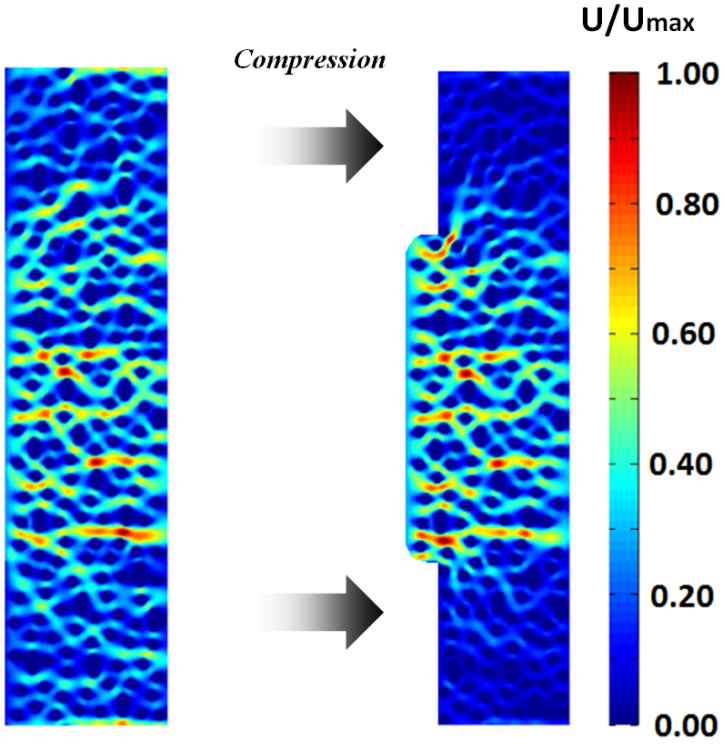

Figure 32. Velocity field in an artificially generated PEFC GDL. (left) Fluid flow behavior when GDL is not under compression. (right) GDL under compression. Note the compression is given only in the land regions. In both cases the porosity, tortuosity and permeability are calculated. Blue color represents low velocities and red color represents high velocities. The channel region is assumed to be linear.

The fluid is allowed to enter to domain in the lattice numbers 101 until 300 in the y- direction. After solving the velocity field using LBM, the tortuosity is calculated using Eq. (56). The porosity is determined using Eq. (55). Two permeability relationships are used for calculating this variable. The comparison of the variables between the initial and final conditions are presented in Table 5.

Table 5. Incidence over the GDL parameters when subjected to compression. Porosity, tortuosity and permeability are compared based on the simulation results. The compression is carried out over the land region.

Variable	*Initial condition* [redacted]	*Final condition* [redacted]	*Relative change*
Channel region thickness [μm]	250	250	NA
Land region thickness [μm]	250	200	- 20.0 %
Porosity [-]	0.7759	0.7546	- 2.7 %
Tortuosity [-]	1.1059	1.1291	+ 2.1 %
[58]Permeability 10^{-12} [m^2]	5.9012	4.7811	- 19.0 %
[59]Permeability 10^{-12} [m^2]	7.5692	5.9779	- 21.0 %

The results show that when the land region of the GDL is compressed around 20 %, the only parameter that increases is the tortuosity (2.1 %). Using two different relationships, i.e., one in which only the porosity is included and another one where the fiber thickness is also considered, the permeability is calculated. Both relationships show a decrement of this variable in around 20 %.

Chapter 6

6 Conclusions and Future Work

This chapter presents the conclusions of the study realized in this Licentiate thesis. The most important findings and the ongoing simulations are mentioned. Additionally, the possible models related to FCs to implement are highlighted.

6.1 Conclusions

The Lattice Boltzmann method has been applied to solve several physical problems at different Re numbers. Solutions of physical problems at macro- and microscale are developed for a 2D case. The 2D flow channel case presents the solution of the velocity field, the entrance length differs with the literature up to 3.00 %, and the velocity profile at different cross sections by using LBM agrees well with the theoretical solution. The velocity and temperature fields were solved for a lid-driven cavity. The deviation error for the velocity field for x- and y- directions was up to 3.91 % and 3.57 %, respectively. The temperature field agrees well with the cited literature. The simulation results using LBM at low Re were analyzed with the flow around a circular obstacle. Three different Re numbers lower than 30 were established, and the ratios between the separated region (s) and the obstacle diameter (d) were determined for validation. The values of the (s/d) ratio vs. Re found in the simulations were compared with data in the literature, and a deviation error lower than 8.0 % was found.

Based on the simulation results and their validations, LBM presented a relatively high accuracy compared to previous studies. LBM has proven to be suitable for solving problems at different scales, and a powerful tool for predicting the fluid flow behavior around obstacles. The fluid flow behavior simulation in porous media related to FCs was obtained. The flow in two artificially generated porous domains, and in one reconstructed domain from a real SEM image were analyzed. Microstructural parameters such as porosity, gas-phase tortuosity and permeability were calculated. Gas-phase tortuosity was determined after using the LBM to solve the velocity field in the porous domain. In the case of the SOFC, the selected region presents a porosity 0.59 and tortuosity 1.18. Using the porosity value found in this work, and replacing it in previous tortuosity-porosity relationships found in the literature yields a deviation error up to 11.0%. To study the variations of the mentioned variables when the GDL in a PEFC is subjected to compression an artificially porous domain was generated based on a realistic GDL. The fluid is allowed to go in the channel region whereas the land region is compressed. The variables are calculated in both, initial and final states of compression. Results show that if the land region is compressed in about 20 %, the porosity decreases by 2.7 % and the tortuosity increase by around 2.0 %. If the permeability is calculated using two different relations found in the literature, this variable decreases up to 21 % of the original value. More studies on this model are required.

6.2 Future Work

Ongoing simulations are related with the transport of species in a porous domain. The artificial porous domain is generated in order to know the distribution of the species concentrations. Figure 33 shows preliminary results of the mentioned model.

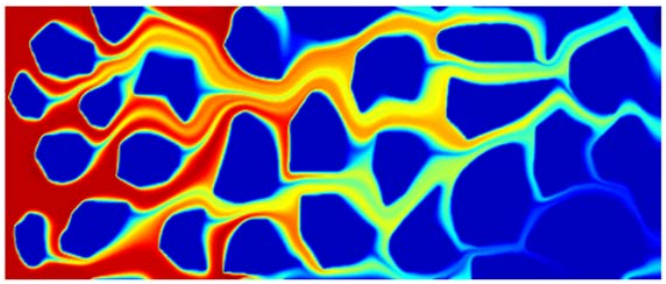

Figure 33. Species concentrations in an artificially generated SOFC anode. The figure shows preliminary results of the species distribution in an artificially generated SOFC anode. Red color represents high value of concentration, blue color lower concentration values. The concentration is defined in left boundary, and no flux is implemented in the right boundary.

Based on the achieved results, more investigations should be carried out in order to get a more realistic multiphysics and multiscale model. Among the next steps to be implemented are:

- Include chemical reactions involved in the energy conversion process
- Include a detailed analysis of the TPB within the porous media
- Simulate the species distributions for more than one species
- Generate a 3D microstructure for modeling the different transport phenomena, and code the LBM for solving phenomena in 3D
- Include phase-change occurring during the energy conversion process
- Apply the parallelization computing in order to take advantage of the LBM's locality
- Couple different layers in the model; such as GDL and CL in PEFCs, and support and active layer in SOFCs

References

[1] Chapman, I. (2014). The End of Peak Oil? Why This Topic is Still Relevant Despite Recent Denials. *Energy Policy*, **64**, 93-101.

[2] Miller, R. G., & Sorrell, S. R. (2014). The Future of Oil Supply. *Philosophical Transactions of the Royal Society of London A: Mathematical, Physical and Engineering Sciences*, **372**(2006), 20130179.

[3] Matthews, H. D. (2014). A Growing Commitment to Future CO2 Emissions. *Environmental Research Letters*, **9**(11), 111001.

[4] Pazheri, F. R., Othman, M. F., & Malik, N. H. (2014). A review on Global Renewable Electricity Scenario. *Renewable and Sustainable Energy Reviews*, **31**, 835-845.

[5] Carter, D., Wing, J. (2013). The Fuel Cell Industry Review 2013. Fuel Cell Today

[6] Farooque, M., & Maru, H.C. (2001). Fuel Cells-the Clean and Efficient Power Generators. *Proceedings of the IEEE* 2001; **89**(12), 1819-1829.

[7] Kirubakaran, A., Jain, S., & Nema, R. K. (2009). A Review on Fuel Cell Technologies and Power Electronic Interface. *Renewable and Sustainable Energy Reviews*, **13**(9), 2430-2440.

[8] Zamel N. (2011). Transport Properties of the Gas Diffusion Layer of PEM Fuel Cells. Ph.D. Thesis, University of Waterloo, Ontario, Canada.

[9] Yoon, Y. G., Park, G. G., Yang, T. H., Han, J. N., Lee, W. Y., & Kim, C. S. (2003). Effect of Pore Structure of Catalyst Layer in a PEMFC on its Performance. *International Journal of Hydrogen Energy*, **28**(6), 657-662.

[10] Zhang, J. (2008). PEM Fuel Cell Electrocatalysts and Catalyst Layers: Fundamentals and Applications. Springer Science & Business Media.

[11] Spiegel, C. (2008). PEM Fuel Cell Modeling and Simulation Using Matlab, Academic Press, Elsevier Inc.

[12] Moon, H., Kim, S. D., Park, E. W., Hyun, S. H., & Kim, H. S. (2008). Characteristics of SOFC Single Cells with Anode Active Layer via Tape Casting and Co-firing. *International Journal of Hydrogen Energy*, **33**(11), 2826-2833.

[13] Lee, H. K., Park, J. H., Kim, D. Y., & Lee, T. H. (2004). A Study on the Characteristics of the Diffusion Layer Thickness and Porosity of the PEMFC. *Journal of Power Sources*, **131**(1), 200-206.

[14] Russell, J. B. (2003). Investigation of the Effect of Catalyst Layer Composition on the Performance of PEM Fuel Cells. Ph.D. Thesis, Virginia Polytechnic Institute and State University, Virginia, USA

[15] Kong, J., Sun, K., Zhou, D., Zhang, N., Mu, J., & Qiao, J. (2007). Ni–YSZ Gradient Anodes for Anode-supported SOFCs. *Journal of Power Sources*, **166**(2), 337-342.

[16] Williford, R. E., Chick, L. A., Maupin, G. D., Simner, S. P., & Stevenson, J. W. (2003). Diffusion Limitations in the Porous Anodes of SOFCs. *Journal of the Electrochemical Society*, **150**(8), A1067-A1072.

[17] Simwonis, D., Thülen, H., Dias, F. J., Naoumidis, A., & Stöver, D. (1999). Properties of Ni/YSZ Porous Cermets for SOFC Anode Substrates Prepared by Tape Casting and Coat-mix® Process. *Journal of Materials Processing Technology*, **92**, 107-111.

[18] Espinoza, M., Sundén, B., & Andersson, M. (2014). Highlights of Fuel Cell Modeling From a Lattice Boltzmann Method Point of View. In *ASME 2014 International Mechanical Engineering Congress & Exposition* (pp. V06AT07A058-V06AT07A058). American Society of Mechanical Engineers. Paper No. IMECE2014-37010

[19] Grew, K. N., & Chiu, W. K. (2012). A Review of Modeling and Simulation Techniques Across the Length Scales for the Solid Oxide Fuel Cell. *Journal of Power Sources*, **199**, 1-13.

[20] Andersson, M., Yuan, J., & Sundén, B. (2010). Review on Modeling Development for Multiscale Chemical Reactions Coupled Transport Phenomena in Solid Oxide Fuel Cells. *Applied Energy*, **87**(5), 1461-1476.

[21] Joshi, A. S., Grew, K. N., Peracchio, A. A., & Chiu, W. K. (2007). Lattice Boltzmann Modeling of 2D Gas Transport in a Solid Oxide Fuel Cell Anode. *Journal of Power Sources*, **164**(2), 631-638.

[22] Paradis, H., Andersson, M., & Sundén, B. (2013). Perspectives on Lattice Boltzmann Modeling of Transport Processes with Electrochemical Reactions in SOFCs. In *ASME 2013 International Mechanical Engineering Congress and Exposition* (pp. V06BT07A014-V06BT07A014). American Society of Mechanical Engineers. Paper No. IMECE2013-62159

[23] Yan, Y. Y., Zu, Y. Q., & Dong, B. (2011). LBM, a Useful Tool for Mesoscale Modelling of Single-phase and Multiphase Flow. *Applied Thermal Engineering*, **31**(5), 649-655.

[24] Espinoza, M., Sundén, B., & Andersson, M. (2014). Lattice Boltzmann Modeling From the Macro-to the Microscale-An Approximation to the Porous Media in Fuel Cells. In *REGenerative Energien und WAsserstofftechnologie-Symposium, REGWA 2014*.

[25] Sayed, A. M., Hussein, M. A., & Becker, T. (2010). An Innovative Lattice Boltzmann Model for Simulating Michaelis–Menten-based Diffusion–advection Kinetics and its Application within a Cartilage cell Bioreactor. *Biomechanics and Modeling in Mechanobiology*, **9**(2), 141-151.

[26] Bhatnagar, P. L., Gross, E. P., & Krook, M. (1954). A Model for Collision Processes in Gases. I. Small Amplitude Processes in Charged and Neutral One-component Systems. *Physical Review*, **94**(3), 511.

[27] Mohamad, A. A. (2011). Lattice Boltzmann Method: Fundamentals and Engineering Applications with Computer Codes. Springer Science & Business Media.

[28] Succi, S. (2001). The Lattice-Boltzmann Equation (pp. 145-197). Oxford University Press, Oxford.

[29] Zou, Q., & He, X. (1997). On Pressure and Velocity Boundary Conditions for the Lattice Boltzmann BGK Model. *Physics of Fluids (1994-present)*, **9**(6), 1591-1598.

[30] Sukop, M. C., & Thorne Jr, D. T. (2006). Lattice Boltzmann Modeling: An Introduction for Geoscientists and Engineers. ISBN 3540279814.

[31] Inamuro, T., Yoshino, M., & Ogino, F. (1995). A Non-slip Boundary Condition for Lattice Boltzmann Simulations. *Physics of Fluids (1994-present)*, **7**(12), 2928-2930.

[32] Paradis, H. (2013). Micro- and Macroscale Modeling of Transport Processes in Solid Oxide Fuel Cells, Ph.D. Thesis, Lund University, Lund, Sweden.

[33] Huber, C., Chopard, B., & Manga, M. (2010). A Lattice Boltzmann Model for Coupled Diffusion. *Journal of Computational Physics*, **229**(20), 7956-7976

[34] Bernsdorf, J. M. (2008). Simulation of Complex Flows and Multi-physics with the Lattice-Boltzmann Method. Ph.D. Thesis, University of Amsterdan, Netherlands.

[35] Parmigiani, A. (2011). Lattice Boltzmann Calculations of Reactive Multiphase Flows in Porous Media. Ph.D. Thesis, University of Geneva, Switzerland.

[36] Shan, X., & Doolen, G. (1996). Diffusion in a Multicomponent Lattice Boltzmann Equation Model. *Physical Review E*, **54**(4), 3614.

[37] Huber, C., Parmigiani, A., Chopard, B., Manga, M., & Bachmann, O. (2008). Lattice Boltzmann Model for Melting with Natural Convection. *International Journal of Heat and Fluid Flow*, **29**(5), 1469-1480.

[38] Lehnert, W., Meusinger, J., & Thom, F. (2000). Modelling of Gas Transport Phenomena in SOFC Anodes. *Journal of Power Sources*, **87**(1), 57-63.

[39] Andersson, M., Paradis, H., Yuan, J., & Sundén, B. (2011). Review of Catalyst Materials and Catalytic Steam Reforming Reactions in SOFC anodes. *International Journal of Energy Research*, **35**(15), 1340-1350.

[40] Schlichting, H., Gersten, K., & Gersten, K. (2000). Boundary-layer Theory. Springer Science & Business Media.

[41] Sundén, B. (2012). Introduction to Heat Transfer. WIT Press.

[42] Durst, F., Ray, S., Ünsal, B., & Bayoumi, O. A. (2005). The Development Lengths of Laminar Pipe and Channel Flows. *Journal of Fluids Engineering*, **127**(6), 1154-1160.

[43] Ghia, U. K. N. G., Ghia, K. N., & Shin, C. T. (1982). High-Re Solutions for Incompressible Flow Using the Navier-Stokes Equations and a Multigrid Method. *Journal of Computational Physics,* **48**(3), 387-411.

[44] Batchelor, G. K. (2000). An Introduction to Fluid Dynamics. Cambridge University Press.

[45] Li, X. (2011). Green Energy. Springer.

[46] Guo, Z., & Zhao, T. S. (2005). Lattice Boltzmann Simulation of Natural Convection with Temperature-dependent Viscosity in a Porous Cavity. *Progress in Computational Fluid Dynamics, an International Journal*, **5**(1), 110-117.

[47] Nabovati, A., & Sousa, A. C. M. (2007). Fluid Flow Simulation in Random Porous Media at Pore Level Using the Lattice Boltzmann Method. *Journal of Engineering Science and Technology*, **2**(3), 226-237.

[48] Yuan, J., & Sundén, B. (2014). On Mechanisms and Models of Multi-component Gas Diffusion in Porous Structures of Fuel Cell Electrodes. *International Journal of Heat and Mass Transfer*, **69**, 358-374.

[49] Espinoza, M., Sundén, B., Andersson, M., & Yuan, J. (2014). Analysis of Porosity and Tortuosity in a 2D Selected Region of Solid Oxide Fuel Cell Cathode Using the Lattice Boltzmann Method. In Fuel Cell Seminar & Energy Exposition. ECS Trans. 2015 volume 65, issue **1**, 59-73.

[50] Koponen, A., Kataja, M., & Timonen, J. (1996). Tortuous Flow in Porous Media. *Physical Review E*, **54**(1), 406.

[51] Koponen, A., Kataja, M., & Timonen, J. (1997). Permeability and Effective Porosity of Porous Media. *Physical Review E*, **56**(3), 3319.

[52] Barrande, M., Bouchet, R., & Denoyel, R. (2007). Tortuosity of Porous Particles. *Analytical Chemistry*, **79**(23), 9115-9121.

[53] Hottinen, T., Himanen, O., Karvonen, S., & Nitta, I. (2007). Inhomogeneous Compression of PEMFC Gas Diffusion Layer: part II. Modeling the Effect. *Journal of Power Sources*, **171**(1), 113-121.

[54] Nakajima, H. (2013). Lattice Boltzmann Modeling of the Gas Diffusion Layer of the Polymer Electrolyte Fuel Cell with the Aid of Air Permeability Measurements. *Mass Transfer - Advances in Sustainable Energy and Environment Oriented Numerical Modeling.* ISBN: 978-953-51-1170-2, InTech, DOI: 10.5772/56363.

[55] Espinoza, M., Andersson, M., Yuan, J., & Sundén, B. (2015). Compress effects on porosity, gas-phase tortuosity, and gas permeability in a simulated PEM gas diffusion layer. *International Journal of Energy Research*, **39**(11), 1528-1536.

[56] Parikh, N., Allen, J. S., & Yassar, R. S. (2012). Microstructure of Gas Diffusion Layers for PEM Fuel Cells. *Fuel Cells*, **12**(3), 382-390.

[57] Chang, D., & Hung, J. (2012). Effects of Channel Depths and Anode Flow Rates on the Performance of Miniature Proton Exchange Membrane Fuel Cells. *International Journal of Applied Science and Engineering*, **10**(4), 273-280.

[58] Van Doormaal, M. A., & Pharoah, J. G. (2009). Determination of Permeability in Fibrous Porous Media Using the Lattice Boltzmann Method with Application to PEM Fuel Cells. *International Journal for Numerical Methods in Fluids*, **59**(1), 75-89.

[59] Hao, L., & Cheng, P. (2009). Lattice Boltzmann Simulations of Anisotropic Permeabilities in Carbon Paper Gas Diffusion Layers. *Journal of Power Sources*, **186**(1), 104-114.